The Astrophysical Journal, 924:95 (22pp), 2022 January 10 https://doi.org/10.3847/1538-4357/ac32bd

Variability and Spectral Characteristics of Three Flaring Gamma-Ray Quasars Observed by VERITAS and Fermi-LAT

C. B. Adams[1], J. Batshoun[2], W. Benbow[3], A. Brill[4,5], J. H. Buckley[6], M. Capasso[1], B. Cavins[7], J. L. Christiansen[8], P. Coppi[9], M. Errando[6], K. A Farrell[10], Q. Feng[1], J. P. Finley[11], G. M. Foote[12], L. Fortson[13], A. Furniss[2], A. Gent[14], C. Giuri[15], D. Hanna[16], T. Hassan[15], O. Hervet[7], J. Holder[12], M. Houck[17,18], T. B. Humensky[4], W. Jin[19], P. Kaaret[20], M. Kertzman[21], D. Kieda[22], F. Krennrich[23], S. Kumar[16], M. Lundy[16], G. Maier[15], C. E McGrath[10], P. Moriarty[24], R. Mukherjee[1], D. Nieto[25], M. Nievas-Rosillo[15], S. O'Brien[16], R. A. Ong[26], A. Oppenheimer[27,28], A. N. Otte[14], S. Patel[20], K. Pfrang[15], M. Pohl[29], R. R. Prado[15], E. Pueschel[15], J. Quinn[10], K. Ragan[16], P. T. Reynolds[30], A. Rhatigan[8], D. Ribeiro[4], E. Roache[3], J. L. Ryan[26], M. Santander[19], G. H. Sembroski[11], D. A. Williams[7], T. J Williamson[12]
(VERITAS Collaboration),
and
J. Valverde[31,32,33,34], D. Horan[33], S. Buson[35], C. C. Cheung[36], S. Ciprini[37,38], D. Gasparrini[39,40], R. Ojha[41], P. van Zyl[42,43]
(Fermi-LAT Collaboration), and
L. Sironi[44]

[1] Department of Physics and Astronomy, Barnard College, Columbia University, New York, NY 10027, USA
[2] Department of Physics, California State University–East Bay, Hayward, CA 94542, USA
[3] Center for Astrophysics | Harvard & Smithsonian, Cambridge, MA 02138, USA
[4] Physics Department, Columbia University, New York, NY 10027, USA
[5] Now at NASA Goddard Space Flight Center, Greenbelt, MD 20771, USA; aryeh.brill@nasa.gov
[6] Department of Physics, Washington University, St. Louis, MO 63130, USA
[7] Santa Cruz Institute for Particle Physics and Department of Physics, University of California, Santa Cruz, CA 95064, USA; ohervet@ucsc.edu
[8] Physics Department, California Polytechnic State University, San Luis Obispo, CA 94307, USA
[9] Yale University, 260 Whitney Avenue, New Haven, CT 06511, USA
[10] School of Physics, University College Dublin, Belfield, Dublin 4, Ireland
[11] Department of Physics and Astronomy, Purdue University, West Lafayette, IN 47907, USA
[12] Department of Physics and Astronomy and the Bartol Research Institute, University of Delaware, Newark, DE 19716, USA
[13] School of Physics and Astronomy, University of Minnesota, Minneapolis, MN 55455, USA
[14] School of Physics and Center for Relativistic Astrophysics, Georgia Institute of Technology, 837 State Street NW, Atlanta, GA 30332-0430, USA
[15] DESY, Platanenallee 6, D-15738 Zeuthen, Germany
[16] Physics Department, McGill University, Montreal, QC H3A 2T8, Canada
[17] Davidson College, 405 North Main Street, Davidson, NC 28035, USA
[18] Department of Civil and Environmental Engineering, University of California, Irvine, CA 92617, USA
[19] Department of Physics and Astronomy, University of Alabama, Tuscaloosa, AL 35487, USA
[20] Department of Physics and Astronomy, University of Iowa, Van Allen Hall, Iowa City, IA 52242, USA
[21] Department of Physics and Astronomy, DePauw University, Greencastle, IN 46135-0037, USA
[22] Department of Physics and Astronomy, University of Utah, Salt Lake City, UT 84112, USA
[23] Department of Physics and Astronomy, Iowa State University, Ames, IA 50011, USA
[24] School of Physics, National University of Ireland Galway, University Road, Galway, Ireland
[25] Institute of Particle and Cosmos Physics, Universidad Complutense de Madrid, E-28040 Madrid, Spain
[26] Department of Physics and Astronomy, University of California, Los Angeles, CA 90095, USA
[27] Hastings High School, 1 Mount Hope Boulevard, Hastings-on-Hudson, NY 10706, USA
[28] University of Chicago, Chicago, IL 60637, USA
[29] Institute of Physics and Astronomy, University of Potsdam, 14476 Potsdam-Golm, Germany, and DESY, Platanenallee 6, D-15738 Zeuthen, Germany
[30] Department of Physical Sciences, Munster Technological University, Bishopstown, Cork, T12 P928, Ireland
[31] Center for Space Sciences and Technology, University of Maryland Baltimore County, Baltimore, MD 21250, USA
[32] NASA Goddard Space Flight Center, Greenbelt, MD 20771, USA
[33] Laboratoire Leprince-Ringuet, École Polytechnique, CNRS/IN2P3, 91128 Palaiseau, France; valverde@llr.in2p3.fr
[34] Department of Astronomy, Columbia University, New York, NY 10027, USA
[35] Julius-Maximilians-Universität, D-97070, Würzburg, Germany
[36] Space Science Division, Naval Research Laboratory, Washington, DC 20375, USA
[37] Istituto Nazionale di Fisica Nucleare (INFN), Sezione di Roma Tor Vergata, Via della Ricerca Scientica 1, I-00133, Roma, Italy
[38] ASI Space Science Data Center (SSDC), Via del Politecnico, 00133, Roma, Italy
[39] Istituto Nazionale di Fisica Nucleare, Sezione di Roma "Tor Vergata," I-00133 Roma, Italy
[40] Space Science Data Center–Agenzia Spaziale Italiana, Via del Politecnico, snc, I-00133, Roma, Italy
[41] NASA HQ, Washington, DC 20546, USA
[42] The University of the Witwatersrand (WITS), South Africa
[43] South African Radio Astronomy Observatory (SARAO), South Africa
[44] Department of Astronomy and Columbia Astrophysics Laboratory, Columbia University, New York, NY 10027, USA
Received 2021 June 15; revised 2021 October 19; accepted 2021 October 22; published 2022 January 17

Abstract

Flat-spectrum radio quasars (FSRQs) are the most luminous blazars at GeV energies but only rarely emit detectable fluxes of TeV gamma rays, typically during bright GeV flares. We explore the gamma-ray variability and spectral characteristics of three FSRQs that have been observed at GeV and TeV energies by Fermi-LAT and VERITAS, making use of almost 100 hr of VERITAS observations spread over 10 yr: 3C 279, PKS 1222+216, and Ton 599. We explain the GeV flux distributions of the sources in terms of a model derived from a stochastic differential equation describing fluctuations in the magnetic field in the accretion disk and estimate the timescales of magnetic flux accumulation and stochastic instabilities in their accretion disks. We identify distinct flares using a procedure based on Bayesian blocks and analyze their daily and subdaily variability and gamma-ray energy spectra. Using observations from VERITAS, as well as Fermi, Swift, and the Steward Observatory, we model the broadband spectral energy distributions of PKS 1222+216 and Ton 599 during very high energy (VHE)–detected flares in 2014 and 2017, respectively, strongly constraining the jet Doppler factors and gamma-ray emission region locations during these events. Finally, we place theoretical constraints on the potential production of PeV-scale neutrinos during these VHE flares.

Unified Astronomy Thesaurus concepts: Gamma-rays (637); Active galaxies (17); Blazars (164); Flat-spectrum radio quasars (2163)

1. Introduction

Blazars are a class of active galactic nuclei (AGN) with jets oriented nearly along our line of sight. This alignment produces beamed emission, so that many blazars show superluminal motion in their jets (e.g., Jorstad et al. 2001) and have a gamma-ray luminosity dominating their bolometric power. In jet models, high-energy electrons in a relativistically outflowing jet, ejected from an accreting supermassive black hole (SMBH), are responsible for the synchrotron radiation seen as the radio-to-UV continuum from blazars (Blandford & Königl 1979). Blazars have a spectral energy distribution (SED) exhibiting a double-humped structure, with low-energy synchrotron and HE gamma ray–peaked components.

Blazars are the most common gamma ray–emitting objects in the extragalactic sky. Observationally, they can be divided into two classes: BL Lacertae (BL Lac) objects, the aligned counterparts to Fanaroff–Riley I radio galaxies, and flat-spectrum radio quasars (FSRQs), the counterparts to Fanaroff–Riley II radio galaxies (Fanaroff & Riley 1974). The FSRQs are low-synchrotron-peaked blazars with a synchrotron peak frequency of less than 10^{14} Hz. The bolometric luminosity of FSRQs is typically greater than that of BL Lac objects. The anticorrelation of synchrotron luminosity with peak frequency is an empirical relationship known as the blazar sequence (Fossati et al. 1998; Nieppola et al. 2008), though its intrinsic validity has been disfavored by more recent work (Keenan et al. 2021). Accordingly, while FSRQs make up only eight of the 79 AGN that have been detected in the TeV band to date,[45] they are more commonly detected at GeV energies, comprising 650 of 2863 AGN detected by the Large Area Telescope (LAT) on board the Fermi Gamma-Ray Space Telescope (Fermi-LAT; Ajello et al. 2020) and dominating the blazar population detected by the Energetic Gamma Ray Experiment Telescope (EGRET) on the Compton Gamma-Ray Observatory (Mukherjee 2001).

The SED of an FSRQ is generally dominated by the gamma-ray emission component, which peaks in the HE (∼GeV) band. The FSRQs are believed to possess several structures producing radiation fields external to the jet, including a broad-line region (BLR) and a dust torus. The TeV detections of FSRQs are particularly interesting because the external radiation fields might be expected to produce increased Compton cooling of electrons and absorb energetic gamma rays by pair production, leading to a cutoff in the gamma-ray spectrum above the GeV band (e.g., Ghisellini et al. 1998).

Blazars have been observed to be variable at all wavelengths and at timescales down to several minutes in both the GeV and TeV bands (Aharonian et al. 2007; Ackermann et al. 2016). However, the physical mechanisms that drive this variability are unclear. Different processes, possibly originating at different locations in the AGN, may drive variable emission occurring at different timescales. By providing an upper bound on the light-crossing time, the timescale of variability constrains the apparent size of the emission region, giving information on the location and mechanism of the gamma-ray emission. While the short variability timescales observed in blazars suggest that the emission may be connected to processes in the central engine or accretion disk, the ability of very high energy (VHE; $\gtrsim$100 GeV) emission to escape the AGN implies an origin further out in the jet, where absorption is reduced (Abeysekara et al. 2015).

Over longer timescales, blazar variability can be studied through the flux distribution describing the relative frequencies of different flux levels. Blazar flux distributions exhibit long tails and have been described using lognormal models (e.g., Giebels & Degrange 2009), which could indicate evidence of an underlying multiplicative physical process. Meyer et al. (2019) fit the flux distributions of six bright FSRQs with a broken power law, though a lognormal distribution was also compatible with their data, and recently, Tavecchio et al. (2020) described the gamma-ray flux variability of those same objects using a model based on a stochastic differential equation (SDE) including both deterministic and stochastic components.

The physical structure and multiwavelength emission mechanisms of a blazar can be further understood by modeling its SED. In leptonic models, the gamma-ray SED component is explained by relativistic electrons and positrons scattering via the inverse Compton process off of a population of lower-energy seed photons, which may be their own emitted synchrotron photons, as in the synchrotron self-Compton process (SSC; Maraschi et al. 1992), or radiation from an external structure, as in the external inverse Compton process (EIC; e.g., Ghisellini & Madau 1996). The EIC seed photons are commonly taken to be radiation fields in the BLR, although this picture has been challenged by the lack of characteristic

[45] http://tevcat.in2p3.fr/

BLR absorption features in the average gamma-ray spectra of Fermi-LAT FSRQs (Costamante et al. 2018).

In hadronic models, however, some or all of the gamma-ray emission is due to relativistic protons emitting via photohadronic processes, proton synchrotron radiation, or other mechanisms, so that relativistic neutrino emission may occur as well. For example, the blazar HE emission may be dominated by synchrotron radiation losses of HE protons (see, e.g., Aharonian 2000; Mücke & Protheroe 2000). Alternatively, neutrinos may be produced by the photohadronic interaction of a proton with a photon, producing pions that quickly decay to gamma rays and neutrinos, that is, $p\gamma \rightarrow \Delta^{+} \rightarrow p\pi^{0}$ or $n\pi^{+}$ (Dermer & Menon 2009). In this case, production of PeV-scale neutrinos requires a target photon population in the X-ray band. The $p\gamma$ process may co-occur with leptonic gamma-ray emission. Under this scenario, FSRQs may be sources of relativistic neutrinos at PeV or even EeV energies (e.g., Gao et al. 2017; Righi et al. 2020). High-energy neutrinos have been detected coming from a direction compatible with the blazar TXS 0506+056 (IceCube Collaboration et al. 2018), which may be an FSRQ masquerading as a BL Lac object (Padovani et al. 2019).

In this paper, we investigate strong gamma-ray flares from three FSRQs at intermediate redshifts. These three sources were continuously monitored by Fermi-LAT (Section 2.2) during the 10 yr period from 2008 to 2018 and observed during periods of high gamma-ray activity by the Very Energetic Radiation Imaging Telescope Array System (VERITAS; Section 2.1). Table 1 provides an overview of the gamma-ray data analyzed in this work.

At a redshift of $z = 0.536$ (Lynds et al. 1965), 3C 279 is one of the most well-studied blazars. It is among the brightest and most variable extragalactic objects in the gamma-ray sky, giving rise to one of the first large-amplitude gamma-ray flares measured by EGRET in 1996 (Wehrle et al. 1998). In recent times, it underwent multiple bright gamma-ray flares in 2014, 2015, and 2018. Notably, during a flare beginning on 2015 June 16, it was detected by the High Energy Stereoscopic System (H.E.S.S.), and Fermi-LAT observed minute-scale variability (Ackermann et al. 2016; Romoli et al. 2017). H.E.S.S. again detected 3C 279 during the flaring states in 2018 January and June (Emery et al. 2019).

At a redshift of $z = 0.432$ (Osterbrock & Pogge 1987), PKS 1222+216, also known as 4C +21.35, has exhibited periods of extreme variability in the VHE gamma-ray band, with VHE detections occurring during gamma-ray flares in 2010 June (Aleksić et al. 2011) and 2014 February and March (Holder 2014).

Finally, Ton 599, at a redshift of $z = 0.725$ (Schneider et al. 2010; see also Burbidge 1968) and also known as 4C +29.45 and B1156+295, entered a months-long GeV high state in 2017 October (Cheung et al. 2017), leading to VHE detections on the nights of 2017 December 15 and 16 (Mirzoyan 2017; Mukherjee 2017).

We describe the observations and data analysis of these sources in Section 2. In Section 3, we examine the long-term variability of these FSRQs and connect it to processes in the accretion disk. Next, we select gamma-ray flares (Section 4) and analyze the short timescale variability (Section 5) and spectra (Section 6) during these events, focusing primarily on 3C 279, the brightest of the three sources in Fermi-LAT. In Section 7, we model the SEDs of PKS 1222+216 and Ton 599 during their respective VHE detections by VERITAS. The observed VHE emission places constraints on the Doppler factor and gamma-ray emission region location during these flares, which we confirm using an independent method in Section 8. In Section 9, we place theoretical constraints on the potential production of PeV-scale neutrinos during these VHE flares. We summarize our conclusions in Section 10. Throughout this paper, a flat ΛCDM cosmology was used, with $H_0 = 69\ \mathrm{km\ s^{-1}\ Mpc^{-1}}$, $\Omega_M = 0.286$, and $\Omega_\Lambda = 0.714$ (Bennett et al. 2014).

2. Observations and Data Analysis

2.1. VERITAS

VERITAS is an array of four imaging atmospheric Cerenkov telescopes located in southern Arizona (30°40′N, 110°57′W, 1.3 km above sea level; Holder 2011). VERITAS preferentially performs observations of FSRQs when they exhibit an elevated flux in other wave bands, as a flare at TeV energies might also be occurring. The VERITAS observations of 3C 279, PKS 1222+216, and Ton 599 that were simultaneous with the HE flares considered here were taken in response to the elevated fluxes reported by Fermi-LAT. VERITAS also carries out short monitoring observations of FSRQs. Because these sources are not believed to be strong emitters of TeV gamma rays except during flares, the primary aim of this monitoring is to self-trigger on serendipitous flares. For 3C 279 and PKS 1222+216, these observations provide VERITAS data corresponding to low states observed by Fermi-LAT.

The total exposure of the VERITAS observations on each of the sources is reported in Table 1. The data were analyzed using a standard VERITAS data analysis package (Maier & Holder 2017) and cross-checked using an independent package (Cogan 2007). Boosted decision trees with soft selection cuts (appropriate for sources with a photon spectral index softer than $\Gamma \approx 3.5$) were used for separating gamma rays from background cosmic rays (Krause et al. 2017). Preliminary analysis results of the VERITAS observations of 3C 279 and PKS 1222+216 in 2013 and 2014 were reported by Errando (2014). These are superseded by the more updated analyses reported here.

2.2. Fermi-LAT

Fermi-LAT detects gamma rays from 20 MeV to above 500 GeV using a pair-conversion technique (Atwood et al. 2009). Fermi-LAT primarily operates in survey mode, during which it scans the entire sky every 3 hr.

We analyzed the Pass 8 data (Atwood et al. 2013; Bruel et al. 2018) in the 10.3 yr period starting on 2008 August 4 (MJD 54,682.7), the start of the Fermi-LAT all-sky survey, as reported in Table 1. We performed an unbinned likelihood analysis of the data using LAT `Fermitools` 1.0.3 and instrument response functions `P8R3_SOURCE_V2`. The energy range from 0.1 to 500 GeV was analyzed, and photons with a zenith angle >90° were excluded to reduce contributions from the Earth's limb. For each source, the region of interest (ROI) considered was the circle of 10° radius surrounding the catalog source position. The background model consisted of, along with galactic (`gll_iem_v06.fits`) and isotropic (`iso_P8R3_SOURCE_V2.txt`) diffuse emission models, all sources in the FL8Y catalog[46] within a 20° circle surrounding the source. This is to ensure that the model would include

[46] https://fermi.gsfc.nasa.gov/ssc/data/access/lat/fl8y/

Table 1
Overview of the Data Sets Presented in This Paper

Source	z	Fermi-LAT (HE Gamma-Ray)					VERITAS (VHE Gamma-Ray)		
		Date Range [UT]	Energy Range [GeV]	Time Binning [days]	No. Bins	Flare Threshold (No. Flares) [ph cm^{-2} s^{-1}]	Energy Threshold[a] [GeV]	Exposure [hr]	No. Obs.
3C 279	0.5362	2008-08-04–2018-12-07	0.1-500	1	3471	4×10^{-6} (10)	200	54.4	139
PKS 1222+216	0.432	2008-08-04–2018-12-07	0.1-500	3	1158	5×10^{-7} (11)	110	34.7	95
Ton 599	0.725	2008-08-04–2018-12-12	0.1-500	7	512	5×10^{-7} (5)	140	8.8	20

Note.
[a] The energy threshold varies for different observations. A typical value is quoted for 3C 279, and the values during the VHE-detected flares are quoted for PKS 1222+216 and Ton 599.

gamma-ray emission from sources outside the ROI that could extend into the ROI due to the size of the point-spread function of the LAT, especially at low energies. We excluded time ranges corresponding to solar flares and gamma-ray bursts in the ROI from the analysis.

When performing the likelihood fit, we iteratively fixed the parameters of the least significant sources (in increasing square powers of natural numbers up to a test statistic, TS, equal to 25) until convergence was reached. Sources with TS values outside the allowed range, usually associated with flux parameter values close to zero, were removed from the model. When fitting individual light-curve and SED points, the spectral parameters were kept fixed to either their catalog values for global analyses or values derived from an analysis of the full flare period for flare analyses, with the diffuse background model normalization parameters left free. We checked that the background model we used is consistent with the 4FGL-DR2 catalog (Abdollahi et al. 2020; Ballet et al. 2020) by comparing these two catalogs and finding no new bright, variable sources in the ROIs of each of the three FSRQs that could significantly impact the analysis of our sources.

Since 3C 279 lies close to the ecliptic, the Sun and Moon contribute diffuse foreground emission in the ROI of this source during certain periods. This is at a level of $\sim 0.5 \times 10^{-6}\,\mathrm{cm^{-2}\,s^{-1}}$ for the Sun (Abdo et al. 2011) and $\sim 1 \times 10^{-6}\,\mathrm{cm^{-2}\,s^{-1}}$ for the Moon (Abdo et al. 2012). The Sun's quiescent gamma-ray emission extends over a 20° radius, so this emission is partially degenerate with the diffuse backgrounds modeled in the likelihood fit. The Moon moves about $13^\circ\ \mathrm{day^{-1}}$, so it appears within a time bin of 1 day as a strip. No contamination is expected during any of the flare states identified in Section 4, since both the Sun and Moon were more than 20° from 3C 279 during these periods.

To our knowledge, the maximum level of contamination due to the proximity of 3C 279 to the ecliptic has not previously been quantified. To do so, we generated extended templates for the Sun and Moon for a 1 day time bin containing the closest approach of the Sun to 3C 279 during the period considered for our analysis (Johannesson & Orlando 2013), that is, the bin containing 2018 October 9, when its annual occultation occurred (Barbiellini et al. 2014). During this time bin, the Sun reached a distance of ≈0°.2 from 3C 279. By coincidence, the Moon passed within 5° of the source during the same interval. The templates accounted for the expected extended emission from the Sun and Moon during a 1 day time bin. When we include these templates in the model file for the likelihood analysis for this bin, we find that the flux of 3C 279 decreases by approximately 28% with respect to that obtained when only the point sources in the ROI and the galactic and isotropic diffuse backgrounds are included. The gamma-ray emission from the quiescent Sun and Moon is expected to vary with the solar cycle. In order to estimate the worst-case contamination, we also chose a selection of time bins during which only the Moon was present. When its diffuse template is included in the analysis, this results in a decrease of the 3C 279 flux by up to 49% with respect to when the template is omitted.

For time bins in which the Sun or Moon is more than 5° from 3C 279, the flux of 3C 279, as returned by the likelihood analysis, does not change significantly when the solar and lunar templates are included. We conclude, therefore, that these contributions show no evidence of being statistically significant when deriving the spectral properties of 3C 279 for the time periods studied in this work. The Sun and Moon each come within 5° of 3C 279 for approximately 11–13 days $\mathrm{yr^{-1}}$. A more complete treatment, beyond the scope of this paper, could include the Sun and Moon as extended sources in the likelihood fits for these time bins to fully account for their emission.

2.3. Swift-XRT

The X-Ray Telescope (XRT) on the Neil Gehrels Swift Observatory is a grazing-incidence focusing X-ray telescope sensitive to photons with energies between 0.2 and 10 keV (Gehrels et al. 2004; Burrows et al. 2005). Swift-XRT observed PKS 1222+216 and Ton 599 during the VHE flares of those sources.

The Swift-XRT data were extracted from the Swift data archive and analyzed using `HEASoft v6.24`. The fluxes and flux errors were deabsorbed using the fixed total column density of Galactic hydrogen, $N_{\mathrm{H}} = 2.29 \times 10^{20}\,\mathrm{cm^{-2}}$ for PKS 1222+216 and $1.89 \times 10^{20}\,\mathrm{cm^{-2}}$ for Ton 599 (Kalberla et al. 2005; Willingale et al. 2013), and the photoelectric cross section $\sigma(E)$ to account for the effects of neutral hydrogen absorption. The deabsorbed X-ray spectrum was fitted with a broken power-law model for PKS 1222+216 and a power-law model for Ton 599.

2.4. Swift-UVOT

The Ultraviolet/Optical Telescope (UVOT) on the Neil Gehrels Swift Observatory is a photon-counting telescope sensitive to photons with energies ranging from about 1.9 to 7.3 eV or 170 to 550 nm (Roming et al. 2005). Swift-UVOT observed PKS 1222+216 and Ton 599 approximately concurrently with Swift-XRT.

The UVOT data were extracted from the Swift data archive and analyzed using `HEASOFT v6.28`. The counts from the sources and background were extracted from regions of a radius of 5″.0 centered on the position of the sources and nearby positions without any bright sources, respectively. The magnitude values of the sources were computed using `uvotsource` and converted to fluxes using the zero-points given by Poole et al. (2008). Extinction corrections were applied following Roming et al. (2009) using the reddening values $E(B-V) = 0.0199$ and 0.0171 (Schlafly & Finkbeiner 2011) for PKS 1222+216 and Ton 599, respectively.

2.5. Steward Observatory

During the first decade of the Fermi mission, the Steward Observatory of the University of Arizona obtained optical polarimetry, photometry, and spectra of the LAT-monitored blazars and Fermi targets of opportunity using the SPOL CCD Imaging/Spectropolarimeter (Smith et al. 2009). We downloaded the spectrophotometric Johnson *V*- and *R*-band magnitudes from the Steward Observatory public archive.[47] These magnitudes were obtained by convolving the flux spectra between 4000 and 7550 Å with a synthetic filter bandpass for the *V* or *R* band, summing the flux, and computing the magnitude difference with a comparison star. Smith et al. (2009) gave the full details of the observations and data reduction. We then converted the magnitude for each bandpass to its equivalent energy flux. Six observations were taken of

[47] http://james.as.arizona.edu/~psmith/Fermi/

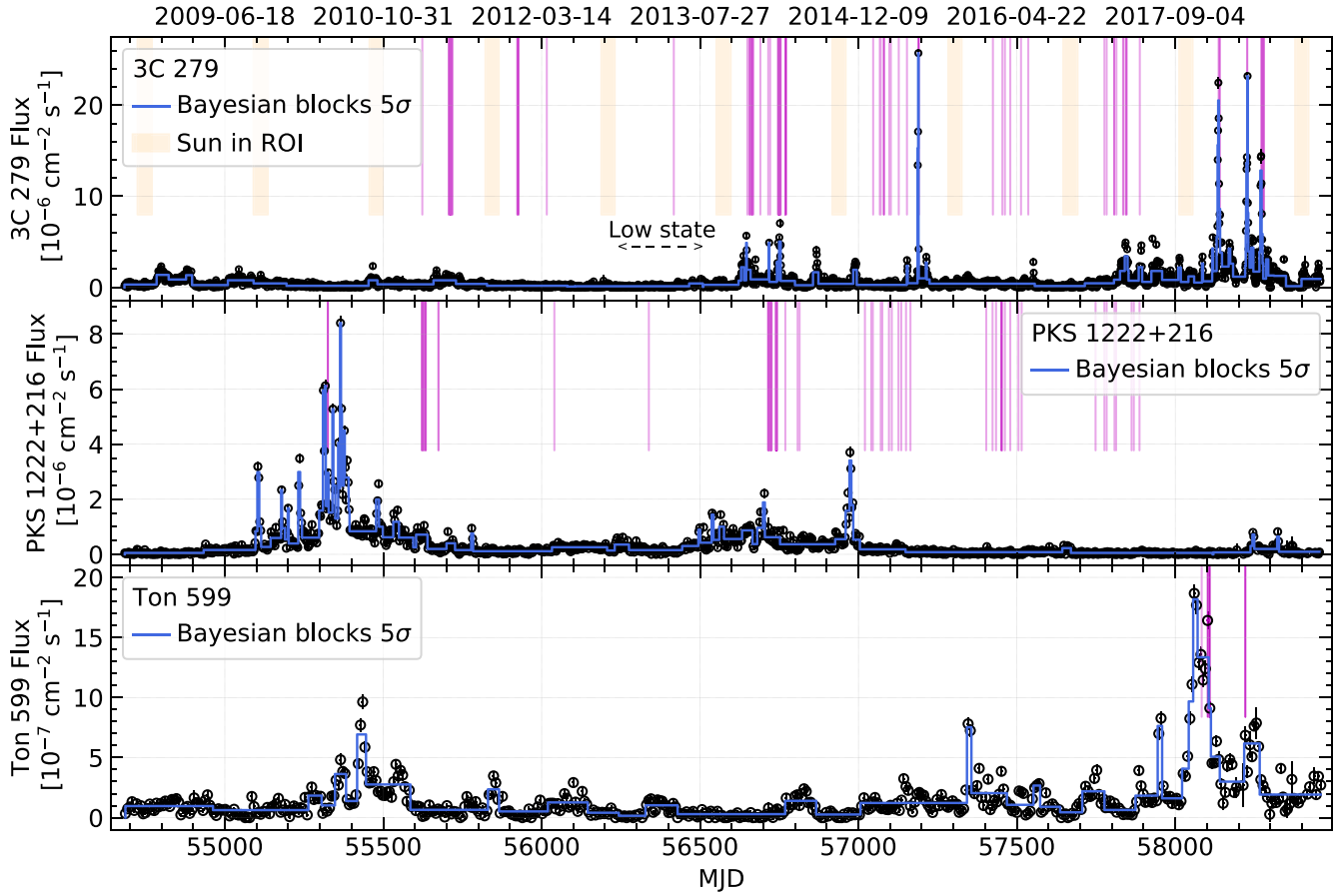

Figure 1. Fermi-LAT light curves of 3C 279 (top), PKS 1222+216 (middle), and Ton 599 (bottom). The flux points (black circles) are shown for 1, 3, and 7 day time bins for the three sources, respectively. The 5σ Bayesian blocks are shown with blue lines. The time intervals in which VERITAS observed the sources are marked in magenta. For 3C 279, the time intervals in which the Sun is less than 20° from the source are shown in orange, and a Fermi-LAT low state from MJD 56,230–56,465 (see Section 6) is marked with a dashed line.

Ton 599 and two of PKS 1222+216 during their respective VHE flares. There was no significant variability during either event.

3. Fermi-LAT Flux Distributions

The Fermi-LAT light curves of the three sources and the periods of the VERITAS observations are shown in Figure 1. The LAT time binnings, reported in Table 1, were chosen for each source depending on its typical strength to avoid having an excessive number of bins with no detection.

The distribution of the LAT fluxes observed from each of these FSRQs may provide a clue to the origin of the gamma-ray emission. The observed flux distributions of the three sources (scaled to form probability density histograms) are shown in Figure 2. Time bins that have a TS less than 9 or that occur when the Sun is less than 20° from the source were excluded.

To account for uncertainties from both the flux binning and the finite observation length, the flux histogram bin errors were calculated using a bootstrapping approach. A total of 2500 bootstrap samples were used, each consisting of the same number of flux points as the actual light curve. Each bootstrap sample was obtained by sampling from the set of actual flux points with replacement, so that a given flux point might be sampled multiple times or not at all.

In order to include the uncertainties of the individual flux points, an error term was added to each sampled point in each bootstrap sample, determined by randomly sampling from a Gaussian distribution with a standard deviation equal to the measurement uncertainty of the respective sampled point. The bin errors were then defined as the standard deviations of the bin fluxes over all of the bootstrap samples binned using the same bins as the original data set.

One form of flux distribution often used to describe blazars is the lognormal distribution (Giebels & Degrange 2009; Sinha et al. 2017; Shah et al. 2018). Lognormal distributions are of interest because they indicate the presence of an underlying multiplicative rather than additive physical process (Aitchison & Brown 1973). Light curves with a lognormal flux distribution have an amplitude of variability linearly proportional to their mean flux.

On the other hand, Tavecchio et al. (2020) proposed an alternative model based on an SDE with two terms modeling a deterministic tendency to return to equilibrium and stochastic fluctuations with an amplitude proportional to the absolute flux level. The form of the SDE is motivated by an astrophysical scenario of stochastic disturbances perturbing a magnetically arrested accretion disk. In this model, the flux distribution is asymmetrical about a peak, falling off as a power law at high fluxes and exponentially at low fluxes, with the relative importance of the deterministic and stochastic components dictating the shape of the distribution. Figure 2 shows a comparison between the best-fit probability density functions (PDFs) corresponding to a lognormal distribution and the

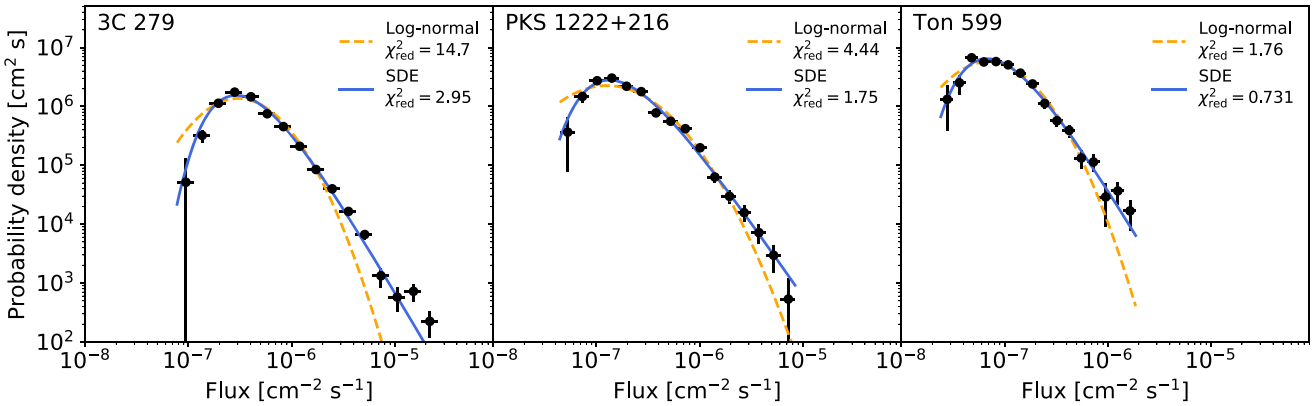

Figure 2. Flux distributions of the three FSRQs, scaled as probability densities. The distributions are fit with a lognormal PDF (dashed orange) and the stationary-state PDF corresponding to the SDE of Tavecchio et al. (2020; solid blue). In all three cases, the SDE provides a better fit.

Table 2
Best-fit Parameters and Goodness of Fit (χ^2_{red}) for the Lognormal and SDE PDF Fits to the LAT Flux Distributions

Source	Lognormal			SDE			
	μ	σ	χ^2_{red}	μ	λ	X_{max}	χ^2_{red}
3C 279	1.65 ± 0.02	0.73 ± 0.01	14.7	8.63 ± 0.28	1.01 ± 0.06	2.90 ± 0.21	2.95
PKS 1222+216	1.07 ± 0.03	0.92 ± 0.03	4.44	6.27 ± 0.60	0.54 ± 0.08	1.33 ± 0.23	1.75
Ton 599	0.21 ± 0.04	0.75 ± 0.03	1.76	2.11 ± 0.19	0.94 ± 0.15	0.68 ± 0.13	0.73

Note. The mean μ and standard deviation σ of the exponentiation of the lognormal distribution and the equilibrium flux μ of the SDE distribution are normalized to 1×10^{-7} ph cm^{-2} s^{-2}. The peak flux of the SDE PDF is given by $X_{max} = \mu\lambda/(\lambda + 2)$.

stationary state of the SDE proposed by Tavecchio et al. (2020).

The stationary-state PDF corresponding to the SDE (Tavecchio et al. 2020, Appendix A) is

$$p(X) = \frac{(\lambda\mu)^{1+\lambda}}{\Gamma(1+\lambda)} \frac{e^{-\lambda\mu/X}}{X^{\lambda+2}}, \quad (1)$$

where X is a dimensionless random variable proportional to the flux, μ is a parameter representing the equilibrium value of X, λ is a parameter representing the relative weight of the deterministic and stochastic terms, and Γ is the gamma function. Here X was related to the flux by a proportionality constant of 1×10^{-7} ph cm^{-2} s^{-1}. The distribution peaks at $X_{max} = \mu\lambda/(\lambda + 2)$. The stationary-state PDF is valid on timescales much longer than the timescale for the system to return to equilibrium, which is clearly the case for the 10 yr periods considered here.

The PDFs were fit to the histogram bins using a nonlinear least-squares algorithm. The best-fit parameters and reduced χ^2 values of the two models are reported in Table 2. In all three cases, the SDE PDF provides a better fit than the lognormal PDF. Both models have two free parameters. We verified that the preference for the SDE model is preserved if the histogram bins at the lowest fluxes, which might be affected by requiring light-curve bins to have a TS >9, are excluded from the fit.

The SDE model PDF is parameterized by the shape parameter $\lambda \equiv 2\theta/\sigma^2$, where θ and σ are the coefficients of the deterministic and stochastic terms. These parameters can be interpreted by associating $1/\theta$ with the timescale of magnetic field accumulation in the accretion disk, while σ is related to the dynamics of the perturbative processes. A large value of λ therefore represents a high relative importance of the deterministic variability component compared to the stochastic one, while a small value indicates the opposite. To relate these timescales to the gravitational radii of the central SMBHs, $r_g = GM/c^2$, we adopt values of $\sim 5 \times 10^8$, 6×10^8, and 3.5×10^8 $M_\odot$ for the black hole masses of 3C 279, PKS 1222+216, and Ton 599, respectively (Hayashida et al. 2015; Farina et al. 2012; Liu et al. 2006).

One can estimate σ^2 from the light curve using the expression (Tavecchio et al. 2020)

$$\sigma^2 \simeq \frac{1}{n} \sum_{i=0}^{n} \frac{(X_i - X_{i-1})^2}{X_{i-1}^2 (t_i - t_{i-1})}, \quad (2)$$

where X_i is the scaled flux at time step i. Using this expression, we obtain σ^2 equal to 0.35, 0.16, and 0.062 day^{-1}, or 100, 200, and 800 r_g/c, for 3C 279, PKS 1222+216, and Ton 599, respectively. These values are consistent with the $\gtrsim 100\, r_g/c$ variability timescale injected into the jet by the magnetorotational instability in the accretion disk estimated in theoretical work (Giannios & Uzdensky 2019). Using the relation $1/\theta = 2/\lambda\sigma^2$, we can then constrain the physics of the accretion flow in 3C 279, PKS 1222+216, and Ton 599 by estimating their magnetic flux accumulation timescales to be 200, 700, and 1800 r_g/c, respectively, within the magnetically arrested disk scenario.

4. Flare Selection

Flare states were identified in the Fermi-LAT data using the following procedure.

1. Segment the data using Bayesian blocks. We set the false-positive rate p_0 to the value equivalent to 5σ using Equation (13) of Scargle et al. (2013).
2. Choose a flux threshold above which the blocks are designated as flaring.
3. Designate each contiguous set of flare blocks as an individual flare state and all nonflare blocks as the quiescent state.

This empirical procedure reflects a picture of individual flares superimposed on a constant quiescent background but identifies them purely as states of elevated flux, making no explicit assumptions about the flares' shape or spectra. Due to its basis on Bayesian blocks, it guarantees that states identified as flares have flux significantly greater than the states surrounding them.

The flux threshold to identify flares must be tuned on a source-by-source basis. Choosing the flux threshold to identify flares involves a trade-off between ensuring that dimmer flares are selected and avoiding misidentifying fluctuations in the quiescent background as flares. In addition, because the sources differ in average flux, the threshold must necessarily vary on an absolute level from source to source. Performing the flare selection procedure with the flare selection thresholds listed in Table 1 results in 10 flares selected for 3C 279, 11 for PKS 1222+216, and five for Ton 599, listed in Table 3. We set the threshold low enough for each source to ensure that all flares that triggered VERITAS observations were selected.

Because the flux distributions are best fit by the single-component SDE model PDF, it is not natural to calculate a duty cycle of flares based on a division into baseline and flaring components (e.g., Resconi et al. 2009). The amount of time spent in the highest-flux states can be estimated directly from the flux distribution by defining the "typical" flux as the peak of the PDF, given in Table 2. Objects 3C 279, PKS 1222+216, and Ton 599 have flux greater than 5 (10) times the typical flux 12% (4%), 19% (8%), and 13% (4%) of the time, respectively.

Our flare selection flux thresholds for 3C 279 and Ton 599 are comparable at 13.8 and 11.8 times their typical fluxes, consistent with their similar values of the PDF shape parameter $\lambda \approx 1$. For PKS 1222+216, our threshold is 3.8 times the typical flux. This source has a lower value of $\lambda \approx 0.5$, with a correspondingly harder power law of the flux distribution at high fluxes. This is perhaps reflected in the long epochs of high flux seen in this source's light curve, such as its flare 3 in 2010, which is approximately 1 yr in duration (Table 3). A relatively low threshold was therefore needed to also capture the smaller flares of the approximately weekly timescales that typically trigger VERITAS observations, consistent with the other two sources.

5. Daily and Subdaily Variability

In order to deduce the smallest variability time around the rising and decaying periods of each flare selected according to the algorithm described in Section 4, we extracted subdaily light curves of the three sources in time bins ranging from 12 hr down to 1.5 hr for the brightest source, 3C 279. Starting from daily time bins, we refined the light curve iteratively by splitting the time bin duration until each bin had a TS of $\gtrsim$50 or until further refinement would not change the local trend of the light curve. For PKS 1222+216 and Ton 599, the minimum bin sizes were 12 and 6 hr, respectively.

Table 3
Fermi-LAT Flares Selected Using the Algorithm Given in Section 4

No.	Date Range (MJD)	Approx. Date	Blocks	VHE Exp.
		3C 279		
1	56,645.66–56,647.66	Dec 2013	1	…
2	56,717.66–56,718.66	Mar 2014	1	…
3	56,749.66–56,754.66	Apr 2014	1	6.79 hr
4	57,186.66–57,190.66	Jun 2015	3	1.00 hr
5	58,116.66–58,119.66	Dec 2017	1	…
6	58,130.66–58,141.66	Jan 2018	4	1.38 hr
7	58,168.66–58,173.66	Feb 2018	1	…
8	58,222.66–58,230.66	Apr 2018	5	0.83 hr
9	58,239.66–58,247.66	May 2018	1	…
10	58,268.66–58,275.66	Jun 2018	2	3.95 hr
		PKS 1222+216		
1	55,096.66–55,114.66	Sep–Oct 2009	3	…
2	55,144.66–55,201.66	Nov–Dec 2009	5	…
3	55,231.66–55,594.66	2010	27	…
4	55,603.66–55,639.66	Feb–Mar 2011	4	5.38 hr
5	55,777.66–55,783.66	Aug 2011	1	…
6	56,494.66–56,500.66	Jul 2013	1	…
7	56,536.66–56,665.66	Sep 2013	5	…
8	56,680.66–56,752.66	Jan–Apr 2014	3	15.53 hr
9	56,926.66–57,004.66	Sep–Dec 2014	5	…
10	58,243.66–58,249.66	May 2018	1	…
11	58,321.66–58,327.66	Jul 2018	1	…
		Ton 599		
1	55,417.66–55,445.66	Aug–Sep 2010	1	…
2	57,342.66–57,356.66	Nov 2015	1	…
3	57,944.66–57,958.66	Jul 2017	1	…
4	58,042.66–58,140.66	Oct 2017–Jan 2018	5	8.30 hr
5	58,217.66–58,266.66	Apr–May 2018	1	2.00 hr

Note. For each enumerated flare, the date range in MJD, approximate calendar date, number of Bayesian blocks, and amount of VHE gamma-ray exposure taken by VERITAS (if any) are provided. All of the times in the date ranges given in Table 1 but not listed here are considered to be quiescent.

To characterize the flares with multiple peaks, we used a sum of the exponential profiles (Valtaoja et al. 1999; Abdo et al. 2010), F_i, where each one has the form

$$F_i(t) = \begin{cases} F_{0_i}\, e^{(t-t_{\mathrm{peak}_i})/t_{\mathrm{rise}_i}}, & t \leqslant t_{\mathrm{peak}_i} \\ F_{0_i}\, e^{-(t-t_{\mathrm{peak}_i})/t_{\mathrm{decay}_i}}, & t > t_{\mathrm{peak}_i}. \end{cases} \quad (3)$$

For flares with a single peak, we used

$$F(t) = \begin{cases} F_0\, e^{(t-t_{\mathrm{peak}})/t_{\mathrm{rise}}} + F_{\mathrm{const}}, & t \leqslant t_{\mathrm{peak}} \\ F_0\, e^{-(t-t_{\mathrm{peak}})/t_{\mathrm{decay}}} + F_{\mathrm{const}}, & t > t_{\mathrm{peak}}, \end{cases} \quad (4)$$

including a constant term to avoid having a bias toward large rise and decay timescales, which is minimal when multiple peaks are included.

The fitting procedure started by considering a single peak characterized by Equation (4). In order to evaluate the possibility of adding a second peak, a fit to the sum of two exponential profiles, as given by Equation (3), was performed and compared against the one-peak scenario using the reduced χ^2 method. The two-peak model was then taken when an improvement was observed over the one-peak function. More peaks were then

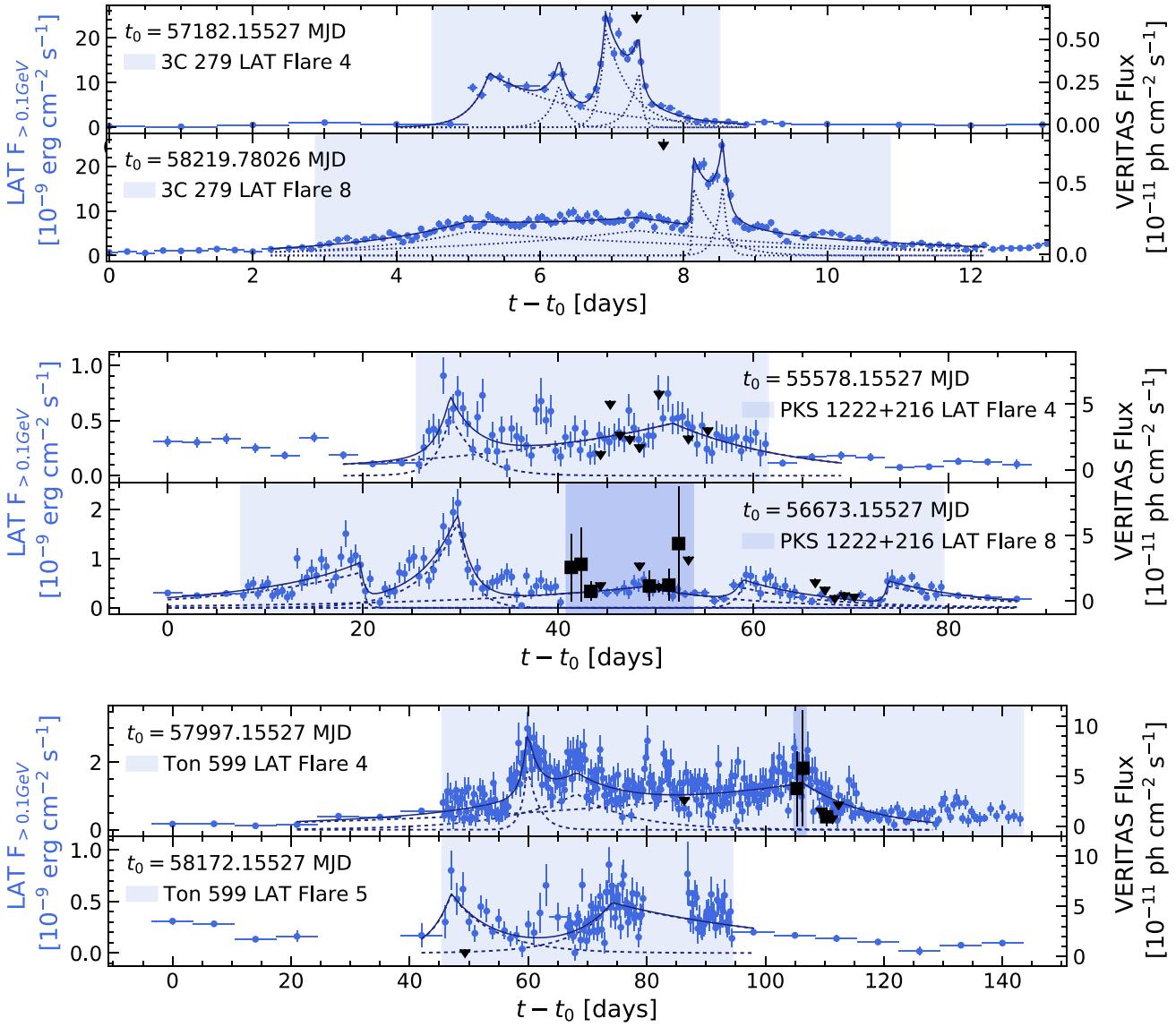

Figure 3. The LAT daily and subdaily light curves (blue points) around selected flaring episodes (light shaded areas). The dotted blue lines show the fitted exponential profiles, with their sums shown in solid blue. The dark shaded areas indicate the periods considered for the SED modeling (Section 7). The VERITAS data points and 95% upper limits are shown as black squares and downward triangles.

added following a similar procedure until a reasonable reduced χ^2 value was reached or the best-fit values obtained no longer provided relevant information for constraining the variability timescales of the sources under study. At each step, human judgment was used to initialize the profile positions and determine by eye that the fits made sense. The peaks were not required to match the Bayesian blocks used for flare selection, which were defined using the coarsely binned light curves.

The flare profiles of the three sources are shown in Figure 3. Two selected flares of 3C 279 are shown, as are the two flares each of PKS 1222+216 and Ton 599 that were observed by VERITAS. Profiles of all 10 flares of 3C 279 are provided in Appendix A. In order to illustrate when VERITAS observed the source relative to the LAT flare peaks, the VERITAS daily-binned light curves for each of the flares are also shown in Figure 3.

The fit results for the three sources are reported in Tables 4, 5, and 8. For 3C 279, each flare lasted between 1 and 11 days and consisted of between one and four separately resolved components, modeled using exponential profiles. Twenty-four distinct components are resolved within the 10 flares. The rise and decay times range from timescales of days to less than 1 hr. The smallest resolved variability timescale was 36 ± 13 minutes, which occurred around MJD 58,227.945, during the rising period of flare 8 (MJD 58,222.655–58,230.655), indicated in bold in Tables 4 and 8.

For PKS 1222+216 and Ton 599, the variability timescales were of the order of days. Notably, for both sources, the fastest variability did not occur during the detected VHE flares. The shortest variability timescale observed by LAT during the VHE flare of PKS 1222+216 was 10.4 ± 6.2 days, which was the decay timescale of the coincident flare component. The shortest variability timescale of Ton 599 observed by LAT during its VHE flare was 11.8 ± 1.1 days, which was also the coincident flare component's decay timescale. In the case of Ton 599, the VERITAS detection occurred over a period of 2 days, after which the observed VHE flux became insignificant. No

Table 4
Results of the LAT Flare Profile Fits for 3C 279 with Flare Timescales in Minutes

Amplitude (F_0) (10^{-9} erg cm^{-2} s^{-1})	t_{peak} (MJD)	t_{rise} (minutes)	t_{decay} (minutes)
Flare 4 (MJD 57,186.655–57,190.655): χ^2/d.o.f. = 77.31/19 = 4.07			
12.07 ± 0.67	57,187.446 ± 0.031	378 ± 46	1784 ± 147
9.79 ± 2.29	57,188.425 ± 0.028	216 ± 101	155 ± 64
21.72 ± 1.59	57,189.069 ± 0.008	137 ± 18	512 ± 55
12.41 ± 1.30	57,189.532 ± 0.010	220 ± 63	77 ± 25
Flare 8 (MJD 58,222.655–58,230.655): χ^2/d.o.f. = 177.25/106 = 1.67			
5.29 ± 1.29	58,224.773 ± 0.105	1996 ± 716	5899 ± 4035
17.70 ± 2.01	58,227.945 ± 0.004	**36 ± 13**	329 ± 131
16.42 ± 1.87	58,228.323 ± 0.012	140 ± 54	115 ± 48
5.59 ± 1.69	58,227.139 ± 0.133	3816 ± 1450	4077 ± 2080

Note. The smallest variability time found is indicated in bold.

Table 5
Results of the LAT Flare Profile Fits for PKS 1222+216 and Ton 599 with Flare Timescales in Days

	Amplitude (F_0) (10^{-9} erg cm^{-2} s^{-1})	t_{peak} (MJD)	t_{rise} (days)	t_{decay} (days)
PKS 1222+216				
Flare 4 (MJD 55,603.7–55,639.7): χ^2/d.o.f. = 102.25/69 = 1.48				
	0.56 ± 0.09	55607.1 ± 0.3	1.5 ± 0.5	2.7 ± 0.8
	0.48 ± 0.03	55629.9 ± 1.2	22.3 ± 3.5	12.1 ± 2.2
Flare 8 (MJD 56,680.7–56,752.7): χ^2/d.o.f. = 166.40/104 = 1.60				
	0.72 ± 0.09	56692.9 ± 0.1	13.6 ± 2.7	0.4 ± 0.3
	1.75 ± 0.17	56702.8 ± 0.2	3.6 ± 0.6	1.5 ± 0.3
*	0.43 ± 0.05	56721.9 ± 1.6	19.9 ± 8.5	**10.4 ± 6.2**
	0.41 ± 0.10	56732.0 ± 0.4	0.9 ± 0.8	8.6 ± 3.6
	0.44 ± 0.06	56746.9 ± 0.1	0.3 ± 0.3	10.3 ± 2.5
Ton 599				
Flare 4 (MJD 58,042.7–58,140.7): χ^2/d.o.f. = 456.78/296 = 1.54				
	1.89 ± 0.29	58057.1 ± 0.2	1.1 ± 0.3	1.9 ± 0.6
	1.06 ± 0.11	58065.4 ± 1.0	11.9 ± 2.6	9.0 ± 2.1
*	1.37 ± 0.06	58103.5 ± 0.8	47.0 ± 4.7	**11.8 ± 1.1**
Flare 5 (MJD 58,217.7–58,266.7): χ^2/d.o.f. = 153.01/96 = 1.59				
	0.57 ± 0.12	58219.2 ± 1.3	3.5 ± 2.8	7.3 ± 2.1
	0.48 ± 0.03	58246.3 ± 0.7	6.6 ± 1.7	34.9 ± 5.6

Note. The flare components coincident with VHE flares are marked with an asterisk * with the corresponding smallest variability times indicated in bold.

significant intraflare variability was observed by Fermi-LAT or VERITAS during either event. Therefore, in the remainder of this work, we take the most constraining variability timescales during the VHE flares of PKS 1222+216 and Ton 599 to be 10 and 2 days, respectively.

The symmetry or asymmetry of flares can provide information on the timescales of the particle acceleration and cooling processes in the emission region (e.g., Abdo et al. 2010). If the cooling time is longer than the light travel time through the emission region, the decay time will be longer than the rise time, producing an asymmetric flare. If the cooling time is shorter than the light travel time, the flare will appear more symmetrical. Flares with a slow rise and fast decay may be produced by relativistic magnetic reconnection (Petropoulou et al. 2016).

Figure 4 shows the fitted rise and decay times for each of the exponential flare components of 3C 279. No clear trend in the flare asymmetry is observable, whether overall, among components within a single flare, or between the components belonging to different flares. Both longer decay times and longer rise times are observed, and many flares appear symmetric. A Wilcoxon signed-rank test (Wilcoxon 1945) finds no significant preference ($p = 0.178$) for flares to have a faster rise time than decay time rather than the reverse. These findings are consistent with previous studies of gamma-ray flares in bright Fermi blazars (e.g., Abdo et al. 2010; Roy et al. 2019).

Models of blazar flares powered by relativistic reconnection predict that flare components produced by large, nonrelativistic plasmoids should have similar fluences to components produced by small, relativistic ones, so that flare components should have similar fluences regardless of their variability timescales (Petropoulou et al. 2016). Figure 5 shows the distributions of the fluences of the components of the 10 flares and the 24 individual flare components of 3C 279. The fluence $\mathcal{F}$ of a flare with exponential components F_i is given by

$$\mathcal{F} = \sum_i F_{0_i}(t_{\rm rise} + t_{\rm decay}). \quad (5)$$

For 3C 279 flares 1, 2, 5, and 7, the best fit is given by a single component plus a constant baseline flux. In these cases, the baseline flux is included in the fluence estimate for consistency with the other flares, approximating the flare duration as $t_{\rm rise} + t_{\rm decay}$, so that the fluence is given by

$$\mathcal{F} = (F_0 + F_{\rm const})(t_{\rm rise} + t_{\rm decay}). \quad (6)$$

The median flare fluence is 2.1×10^{-3} erg cm^{-2}, and the median component fluence is 0.85×10^{-3} erg cm^{-2}. The observed component fluences range over about 1 order of magnitude, as do the flare amplitudes, while the rise and decay timescales span about 2 orders of magnitude. These dynamic ranges are generally compatible with the expectations for plasmoid-powered flares derived from particle-in-cell simulations of relativistic magnetic reconnection (Petropoulou et al. 2016).

The long-term gamma-ray variability study of the three FSRQs presented here is compatible with the extensive flare characteristics study recently carried out by Meyer et al. (2019) on the brightest flares detected by Fermi-LAT. A similar Bayesian block analysis was carried out to identify flares and look for variability on subhour timescales. Consistent with their findings, we find subhour-scale variability in 3C 279, where it was possible to resolve flares in finer time bins, suggesting that extremely compact emission regions may be present within the jet.

6. Gamma-Ray Spectra

Figure 6 shows the LAT energy spectra corresponding to the entire data sets of each of the three sources, along with the VERITAS spectral upper limits for 3C 279. The best-fit spectral parameters are reported in Appendix B. Since all three sources were best fit by a log-parabola model in the 4FGL catalog (Abdollahi et al. 2020), we fit the LAT spectra with this

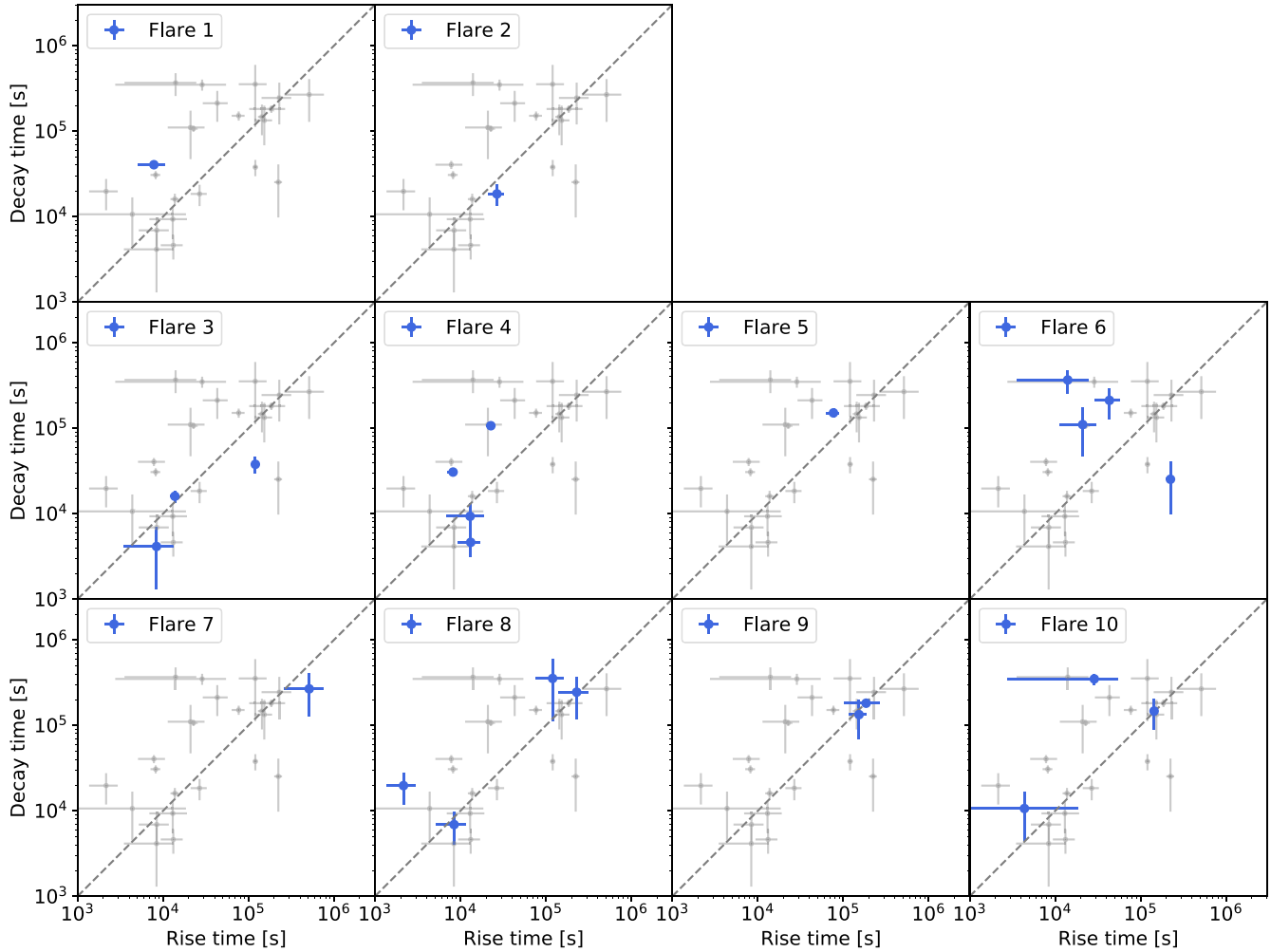

Figure 4. Decay time vs. rise time for each of the resolved exponential components in the flares of 3C 279. The points corresponding to all of the components are shown in gray. The dashed reference line shows where the rise and decay times are equal.

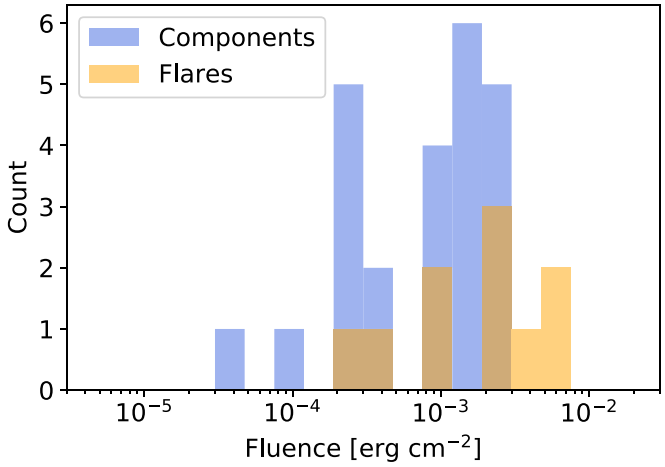

Figure 5. Fluence distributions of the 24 resolved flare components and 10 flares of 3C 279.

model, parameterized as

$$\frac{dN}{dE} = N_0 \left(\frac{E}{E_b}\right)^{-(\alpha+\beta(\log(E/E_b))}, \quad (7)$$

where E_b was fixed to the FL8Y catalog value of 457.698 MeV.

We checked that the log-parabola model provides a better fit than a power-law model using the likelihood ratio test. A power-law subexponential cutoff model was also preferred over a power law, but we could not establish whether this model is significantly preferred with respect to the log-parabola model using a likelihood ratio test. This is because the two curved models are nonnested; i.e., neither is a special case of the other, and therefore it is not possible to calculate the statistical significance of a preference for one over the other. We assumed a log-parabola spectrum for all subsequent LAT analyses. To facilitate comparison with the VERITAS points, the LAT model fits and butterfly contours were extended beyond the LAT maximum energy of 500 GeV, and extragalactic background light (EBL) absorption was applied to them using the model of Franceschini & Rodighiero (2017).

The global spectral shapes of the three sources are similar, with an index α of ∼2.1–2.3 and a curvature parameter β of ∼0.04–0.06, and they differ primarily by their normalization.

Using the data from 3C 279, we compared several methods to determine a baseline nonflaring spectrum. First, we defined a low state lasting from MJD 56,230 to 56,465 (see Figure 1), during which the flux was quiescent and stable in HE gamma rays, *R*-band optical, and X-rays. We checked publicly available Tuorla[48] data for the *R*-band light curve. For the

[48] https://users.utu.fi/kani/1m/3C_279_jy.html

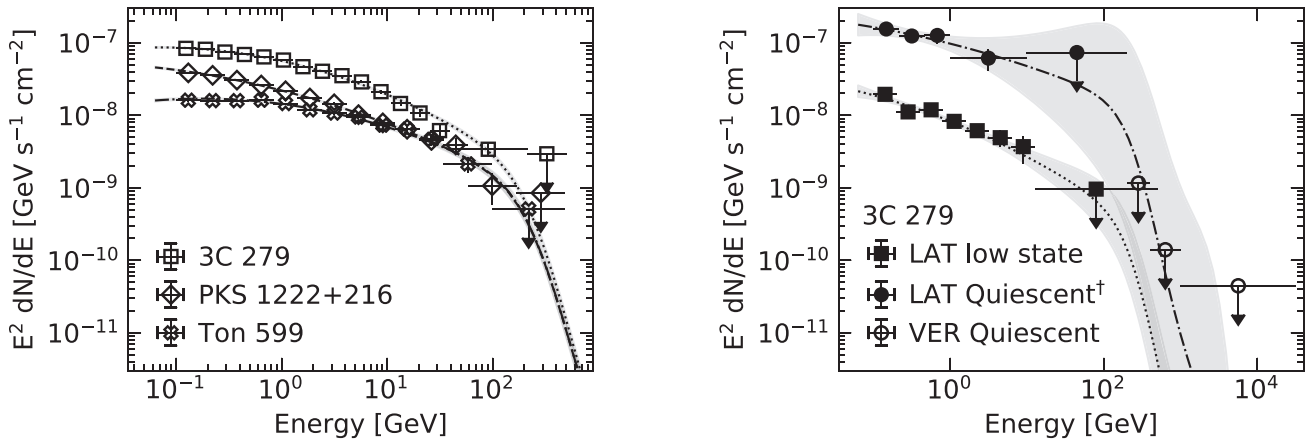

Figure 6. Left: global Fermi-LAT spectra for 3C 279, PKS 1222+216, and Ton 599. The LAT spectra are extrapolated to the VERITAS energy range, incorporating EBL absorption. Right: two baseline states of 3C 279. The Fermi-LAT spectrum corresponding to the multiwavelength low state (MJD 56,230–56,465; see Figure 1) is shown by filled squares. The strictly simultaneous Fermi-LAT spectrum and VERITAS spectral upper limits during the quiescent state are shown by black filled and open circles and contours. The symbol † indicates that the LAT spectrum corresponds to data strictly simultaneous with VERITAS observations. Downward arrows show 95% confidence level upper limits.

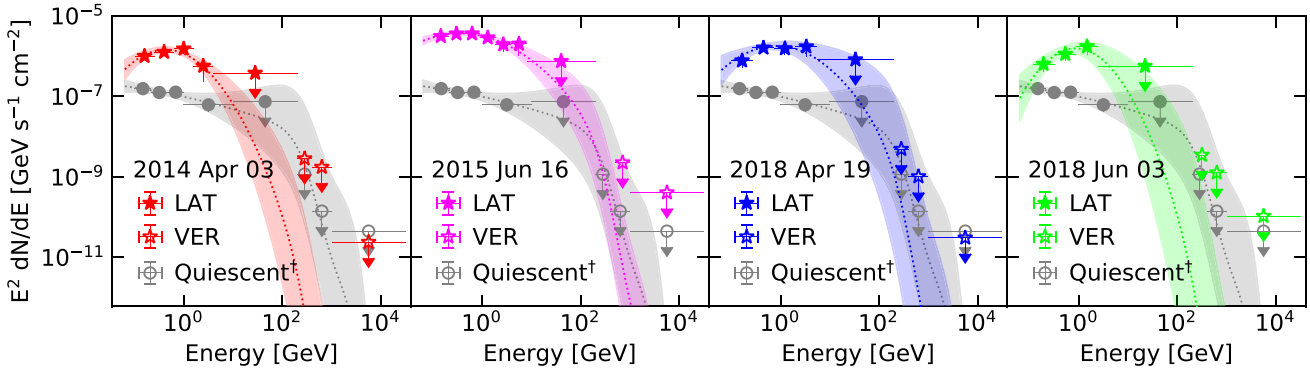

Figure 7. Fermi-LAT spectrum and VERITAS spectral upper limits of 3C 279 during four flares, strictly simultaneous with the VERITAS observations. The quiescent spectrum (gray circles and contour) is shown for comparison. The strictly simultaneous quiescent state LAT data and VERITAS upper limits are represented with filled and open symbols, respectively. The LAT spectra are extrapolated to the VERITAS energy range, incorporating EBL absorption. Downward arrows show 95% confidence level upper limits.

X-rays, we analyzed the Swift-XRT light curve using the online data products generator.[49] To ensure low, stable gamma-ray emission, we selected the interval to span the Bayesian blocks with the lowest flux while excluding intervals with the Sun in the ROI. The low-state LAT SED is shown in Figure 6. Only one VERITAS observation occurred during this interval, on MJD 56,417, so the corresponding VERITAS upper limits are not constraining and are not shown.

Next, using the algorithm proposed in this work and described in Section 4, we designated all epochs of the LAT light curve other than the flaring episodes as quiescent. From those epochs, we extracted those LAT data strictly simultaneous with the VERITAS observations, integrating a total of 43.6 hr of observations. The resulting strictly simultaneous LAT spectrum and VERITAS spectral upper limits are shown in Figure 6. We then performed the same procedure for four flaring epochs during which a significant Fermi-LAT detection could be obtained strictly simultaneously with the VERITAS observations, which occurred on the nights of 2014 April 3, 2015 June 16, 2018 April 19, and 2018 June 3. These strictly simultaneous LAT and VERITAS SEDs are shown in Figure 7.

The spectral shapes of the 3C 279 low and quiescent states are similar to each other and the global state, although the uncertainties on their fit parameters are high due to the low significance. The spectra differ primarily in their flux normalization. The normalization of the low state is lower than that of the global state by design, while the normalization of the strictly simultaneous quiescent state is higher. This could result from the timing of the VERITAS monitoring and triggered observations that often follow up on Fermi-LAT flares and may tend to catch mildly elevated activity in Fermi-LAT even if the source is not actually flaring.

Finally, we derived LAT SEDs for all of the 10 identified flares of 3C 279, using the entire flare time periods, irrespective of strict simultaneity with VERITAS, shown in Figure 8. The average flare spectrum is more strongly curved than the global spectrum, with $\alpha = 2.02 \pm 0.01$ and $\beta = 0.093 \pm 0.008$, compared to $\alpha = 2.228 \pm 0.004$ and $\beta = 0.061 \pm 0.003$ for the global state.

7. SED Modeling

Multiwavelength SED modeling can shed light on the mechanisms of gamma-ray production during VHE flares. For

[49] https://www.swift.ac.uk/user_objects/

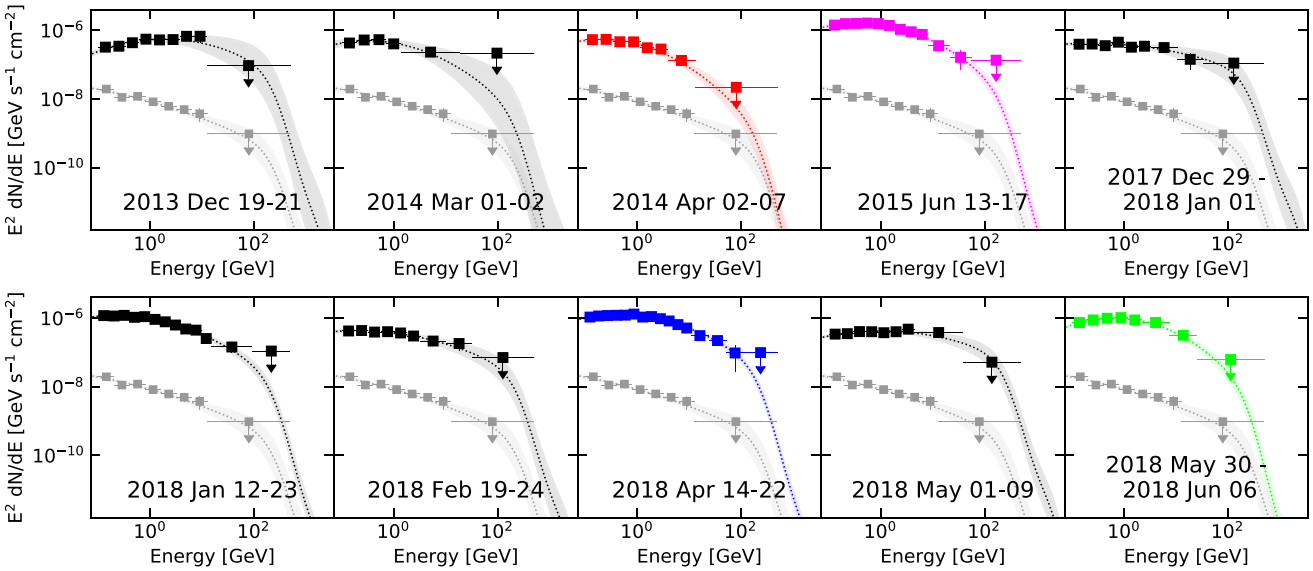

Figure 8. Fermi-LAT spectra of 3C 279 during 10 flares for the intervals selected using the algorithm proposed in this work and described in Section 4. For comparison, the LAT low-state spectrum is shown with gray squares in all of the panels. The four flares shown in color have a corresponding spectrum in Figure 7.

3C 279, we refer the reader to those works in the literature in which multiwavelength SED modeling of the epochs considered here has been performed, and we do not perform any additional modeling (see, for example, Hayashida et al. 2015; Ackermann et al. 2016; Prince 2020; Yoo & An 2020).

Object PKS 1222+216 was first detected at TeV energies by MAGIC during a flaring event in 2010 June (Aleksić et al. 2011), and multiwavelength SED modeling of this event has been performed by, e.g., Tavecchio et al. (2011). We therefore restricted our SED modeling of the source to the duration of the second VHE detection by VERITAS in 2014 February and March. We considered data from all instruments taken from UT 2014 February 26 to 2014 March 10, inclusive.

Ton 599 has not been studied as extensively as the other two sources. Prince (2019) and Patel & Chitnis (2020) modeled its variability characteristics and multiwavelength SED, respectively, during the high state in 2017 December but did not have access to TeV data. We therefore modeled the multiwavelength SED of Ton 599 during the VERITAS detection in 2017 December. We considered data from all instruments taken from UT 2017 December 15 to 2017 December 16, inclusive.

To assemble our multiwavelength SEDs, in addition to the gamma-ray data from VERITAS and Fermi-LAT, we incorporated X-ray and ultraviolet data from the XRT and UVOT instruments on board the Swift satellite and optical observations from the Steward Observatory.

We described the multiwavelength SEDs of the two FSRQs using a multicomponent SSC blob-in-jet model, implemented using the framework of the "`Bjet`" code, developed by Hervet et al. (2015) and based on Katarzyński et al. (2001). We modeled the radiative interactions of a compact leptonic emission zone (a blob), including an EIC emission component resulting from the interactions of the blob particles with the thermal accretion disk emission reprocessed by the BLR. Figure 9 shows a schematic illustration of the components producing the emission in this model.

We consider a simplified BLR model with a normalized density profile based on Nalewajko et al. (2014), where $\rho_{\rm BLR}(r)$

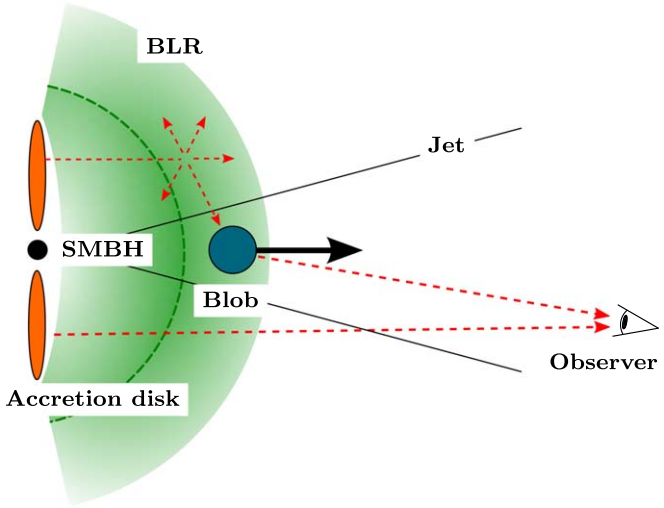

Figure 9. Schematic illustration of the emission model used in this work (not to scale). The green dashed arc represents the nominal BLR radius $r_{\rm BLR}$ corresponding to the region of the maximal BLR density. The observer measures the beamed emission from the blob interacting with the BLR, as well as the accretion disk's thermal emission. The accretion disk is assumed to be a point source.

is at a maximum at the characteristic BLR radius $r = r_{\rm BLR}$ and decreasing as r^{-2} with the distance to the core such that

$$\rho_{\rm BLR}(r) = \frac{(r/r_{\rm BLR})^2}{1 + (r/r_{\rm BLR})^4}\,, \tag{8}$$

with $r_{\rm BLR}$ scaled to the bolometric disk luminosity L_d as $r_{\rm BLR} = 0.1\sqrt{L_d/1 \times 10^{46}\,{\rm erg\,s^{-1}}}$ pc (Sikora et al. 2009; Ghisellini & Tavecchio 2009). From SED modeling of PKS 1222+216 and Ton 599, we deduce BLR radii of 0.17 and 0.15 pc, respectively. We assume an isotropic diffusion of the disk light by the BLR, where the specific intensity of this

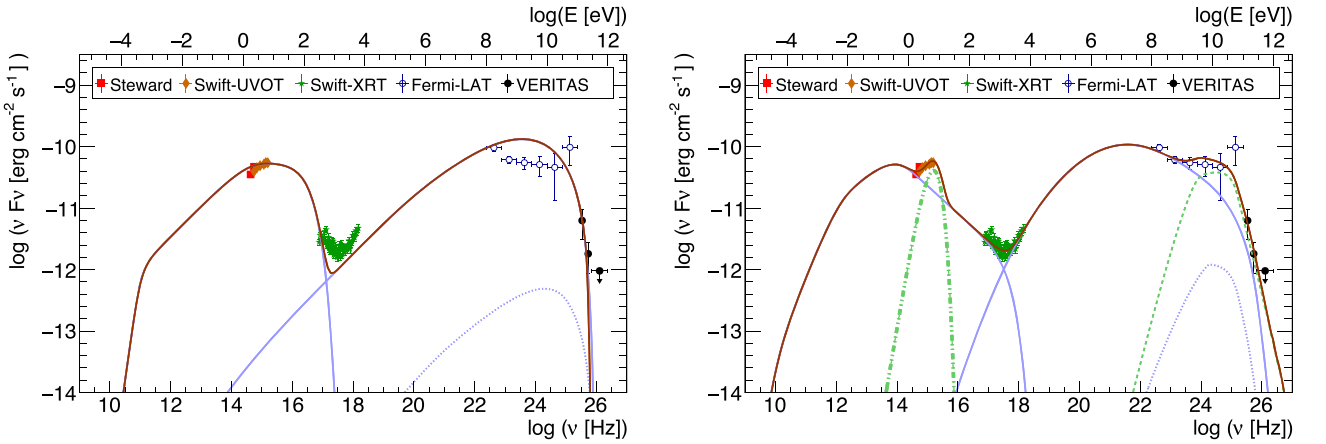

Figure 10. Broadband SED of PKS 1222+216 during the VERITAS detection from UT 2014 February 26 to 2014 March 10. Left: pure SSC model. Right: model considering an EIC component at HE from the interaction of blob particles with the thermal accretion disk emission reprocessed by the BLR. The solid blue lines show synchrotron and SSC emission, the dotted blue line shows second-order self-Compton emission, the heavy dashed green line shows thermal emission from the accretion disk, and the dashed green line shows inverse Compton emission from the BLR. The EBL absorption is taken into account considering the model of Franceschini & Rodighiero (2017).

field can be expressed as

$$I_{\rm BLR}(\nu, T_d, r) = \epsilon_{\rm BLR}\rho_{\rm BLR}(r)\frac{L_d}{4\pi r^2}\frac{I_p(\nu, T_d)}{(\sigma_{\rm SB}/\pi)T_d^4}, \quad (9)$$

where $\sigma_{\rm SB}$ is the Stefan–Boltzmann constant, I_p is the Planck intensity, and $\epsilon_{\rm BLR}$ is the covering factor. This equation is similar to Equation (12) in Hervet et al. (2015) with the addition of the BLR density profile. Only the extension of the BLR in front of the blob plays a significant role in our modeling, since it drives the number of gamma rays produced by the blob that will be absorbed by pair production. The BLR is by default defined between $r = 0$ and $100\,r_{\rm BLR}$. Given the fast convergence of the BLR opacity ($I_{\rm BLR} \propto r^{-4}$), the maximum extension of the BLR does not play a significant role in the model. Although we assume for simplicity that the BLR is isotropic, any anisotropy should have a small effect on the opacity (e.g., Abolmasov & Poutanen 2017, Figure 14).

Figures 10 and 11 show the multiwavelength SED models of PKS 1222+216 and Ton 599. In these figures, the synchrotron and SSC emission are shown by solid blue lines. The subdominant second-order self-Compton emission caused by the interactions of the electrons with the self-Compton photons is shown by a dotted blue line. The thermal emission from the accretion disk is modeled as a point source radiating as a blackbody and is shown by a heavy dashed green line. The inverse Compton emission due to the interaction of the electrons with the disk photons reprocessed in the BLR is shown by a dashed green line. Table 6 gives the parameters characterizing the SED models.

Our model does not include any secondary radiation from pair cascades produced by the absorption of gamma rays in the BLR. While detailed modeling of this effect is beyond the scope of this paper, we estimate that the potential contribution of such cascades would be $\ll$1% of the total bolometric luminosity for PKS 1222+216 and $\lesssim$1% for Ton 599, given the respective levels of absorption in our models, which are described below. We evaluated these contributions by comparing the radiative output of each model with that from the same model with the BLR opacity set to zero. This effect may be noted as a source of systematic uncertainty when interpreting our results.

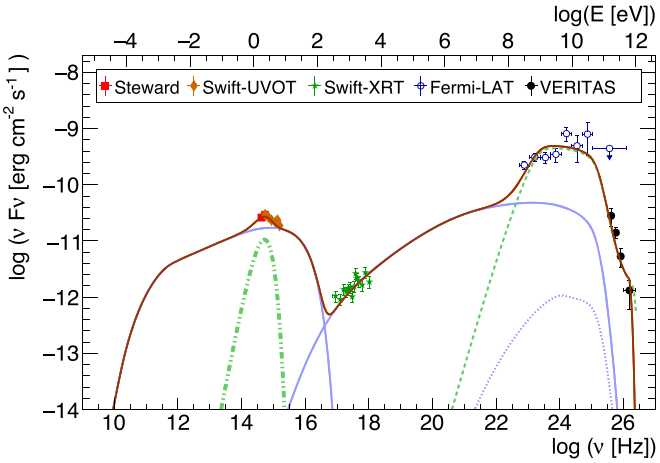

Figure 11. Broadband SED of Ton 599 during the VERITAS detection from UT 2017-12-15 to 2017-12-16. The solid blue lines show synchrotron and SSC emission, the dotted blue line shows second-order self-Compton emission, the heavy dashed green line shows thermal emission from the accretion disk, and the dashed green line shows inverse Compton emission from the BLR.

We note that our model requires that the dust torus luminosity be negligible compared to the disk luminosity. As evidence of far-infrared dust torus thermal emission is lacking in the SED, we consider this assumption to be reasonable in our study. Observing campaigns with good microwave-to-IR coverage would be needed to fully confirm this approach. The presence of strong dust torus emission would require the gamma-ray emission zone to be farther downstream in the jet so as not to produce too large an opacity by pair production.

7.1. PKS 1222+216 Modeling

In order to investigate the necessity of including an EIC component, we represented the multiwavelength SED of PKS 1222+216 with a one-zone pure SSC model, shown in Figure 10 (left). As can be seen by the similar amplitudes of the synchrotron and inverse Compton peaks in the figure, the SED is only weakly Compton-dominated, with the inverse Compton

Table 6
Parameters of the SED Models

Parameter	PKS 1222+216	Ton 599	Unit
θ_{obs}	1.0	1.0	deg
Blob			
δ	40	53	
$N_e^{(1)}$	2.0×10^4	2.7×10^5	cm^{-3}
n_1	2.1	2.5	–
n_2	3.9	3.0	–
γ_{min}	5.5×10^2	3.0×10^2	–
γ_{max}	3.0×10^5	7.0×10^4	–
γ_{brk}	5.0×10^3	1.5×10^4	–
B	3.0×10^{-2}	3.0×10^{-2}	G
R	5.5×10^{16}	6.0×10^{16}	cm
D_{BH}[a]	3.56	2.33	pc
Nucleus			
L_{disk}	2.8×10^{46}	2.2×10^{46}	$erg\ s^{-1}$
T_{disk}	2.8×10^4	1.1×10^4	K
ϵ_{BLR}	2.0×10^{-2}	2.0×10^{-2}	–

Note. Here θ_{obs} is the angle of the blob direction of motion with respect to the line of sight. The electron energy distribution between Lorentz factors γ_{min} and γ_{max} is given by a broken power law with indices n_1 and n_2 below and above γ_{brk}, with $N_e^{(1)}$ the normalization factor at $\gamma = 1$. The blob Doppler factor, magnetic field, radius, and distance to the black hole are given by δ, B, R, and D_{BH}, respectively. The disk luminosity and temperature are given by L_{disk} and T_{disk}, while ϵ_{BLR} is the covering factor of the BLR.
[a] Host galaxy frame.

luminosity about twice the synchrotron luminosity. The Swift-XRT spectrum contains a well-resolved break showing the transition between synchrotron and inverse Compton-dominated emission, which sets a strong constraint on the model. Our best attempt does not provide a satisfying representation of the observed SED. The main issue is that the optical–to–X-ray components of the SED have steep slopes that would require a narrow, sharp synchrotron bump to achieve a good representation, while the X-ray to VHE needs a wide, flat inverse Compton bump. This is not compatible with the usual simple SSC framework, especially when the SED is not heavily Compton-dominated.

In our EIC model, the IR-to-UV SED is dominated by the blackbody big blue bump emission of an accretion disk (see Figure 10, right), which resolves the tension by eliminating the constraint on the synchrotron spectral shape. This allows for a broad SSC component matching the spectral break observed in the X-ray band. In this scenario, the VHE emission is produced by the EIC process between a relativistic blob and the disk thermal emission reprocessed by the BLR. The blob is set to a distance of 3.56 pc from the SMBH, corresponding to 21.3 r_{BLR}. It should be noted that a thermal EIC process was also favored in previous models of PKS 1222+216 where clear disk emission and a strongly Compton-dominated SED were observed during a major outburst in 2010 (Tavecchio et al. 2011).

Because the peak frequency of the EIC emission is directly proportional to the blob Lorentz factor, this scenario imposes a strong constraint on the jet parameters. For PKS 1222+216, in order to match the VHE spectrum, the bulk Lorentz factor needs to be above approximately 23, which was achieved by assuming a Doppler factor $\delta = 40$ and an angle with the line of sight $\theta_{obs} = 1°$. This assumption is consistent with the jet constraints derived by Hervet et al. (2016) from the fastest motion observed in the radio jet of PKS 1222+216, which led to estimations of $\theta_{obs} = 1.°3$, $\delta = 41.3$, and $\Gamma = 29.2$.

Because no significant variability was observed in any wave band during the time period selected for modeling for either source, we considered a stationary model giving a snapshot of the observed activity. As a consistency check, we compared the expected radiative cooling time from the model with the observed flare decay timescale. The cooling time associated with the full radiative output (synchrotron, SSC, and EIC emissions) can be expressed in the Thomson regime as

$$T_{cool}(\gamma) = \frac{3 m_e c}{4 \sigma_T \gamma (U'_B + U'_{syn} + U'_{blr})}, \quad (10)$$

with m_e the electron mass, σ_T the Thomson cross section, γ the Lorentz factor of the emitting particle, and U'_B, U'_{syn}, and U'_{blr}, respectively, the energy density in the blob frame of the magnetic, synchrotron, and external BLR fields (e.g., Inoue & Takahara 1996). One can associate the energy at the break of the spectral particle distribution γ_{brk} with the emission at the peaks of the SED. The Fermi-LAT energy range being mostly above this peak, we can deduce $T_{cool}(\text{Fermi}) \lesssim 17$ days. This is consistent with the observed Fermi-LAT flare decay of 10.4 ± 6.2 days.

The minimum possible variability predicted by our model is 18 hr, given by the blob's radius and Doppler factor such that $\tau_{min} = R(1+z)/(c\delta)$. The total power of the jet is approximately 3.4×10^{45} erg s^{-1} in a particle-dominated regime with the equipartition parameter $U_B/U_e = 1.7 \times 10^{-3}$.

7.2. Ton 599 Modeling

Contrary to PKS 1222+216, the SED of Ton 599 is heavily Compton-dominated, with a ratio of inverse Compton to synchrotron luminosity of approximately 1 order of magnitude. This is a usual signature of an EIC component dominating the gamma-ray emission. We therefore consider the same scenario as for PKS 1222+216. As shown in Figure 11, the model describes the data well.

As in the case of PKS 1222+216, the thermal EIC emission imposes strong constraints on the properties of the emitting region. The largest constraint comes from the gamma-ray opacity by pair creation from the luminous thermal field surrounding the blob. We found that only for a Doppler factor of $\gtrsim$50 is the EIC emission at VHE strong enough to produce the observed VHE gamma rays, given the BLR opacity.

The solution presented in Figure 11, with $\delta = 53$, is consistent with a maximum VHE emission undergoing strong BLR absorption ($E_{max} = 630$ GeV), with an opacity of $\tau_{\gamma\gamma, E_{max}} = 2.8$. In this scenario, we set the blob at a distance of 2.33 pc from the SMBH, corresponding to 15.7 r_{BLR}.

By applying the same consistency check for variability as PKS 1222+216, we found a minimal possible variability timescale predicted by the model of 18 hr (coincidentally, the same as PKS 1222+216) and a radiative cooling time $T_{cool}(\text{Fermi}) \simeq 8.7$ days, in good agreement with the observed Fermi-LAT flare decay of 11.8 ± 1.1 days. The VERITAS observed variability can be associated with the cooling time $T_{cool}(\gamma_{max})$, which leads to $T_{cool}(\text{VERITAS}) = 45$ hr, fully compatible with the observed variability of ~2 days. The blob is estimated to have a total power of approximately

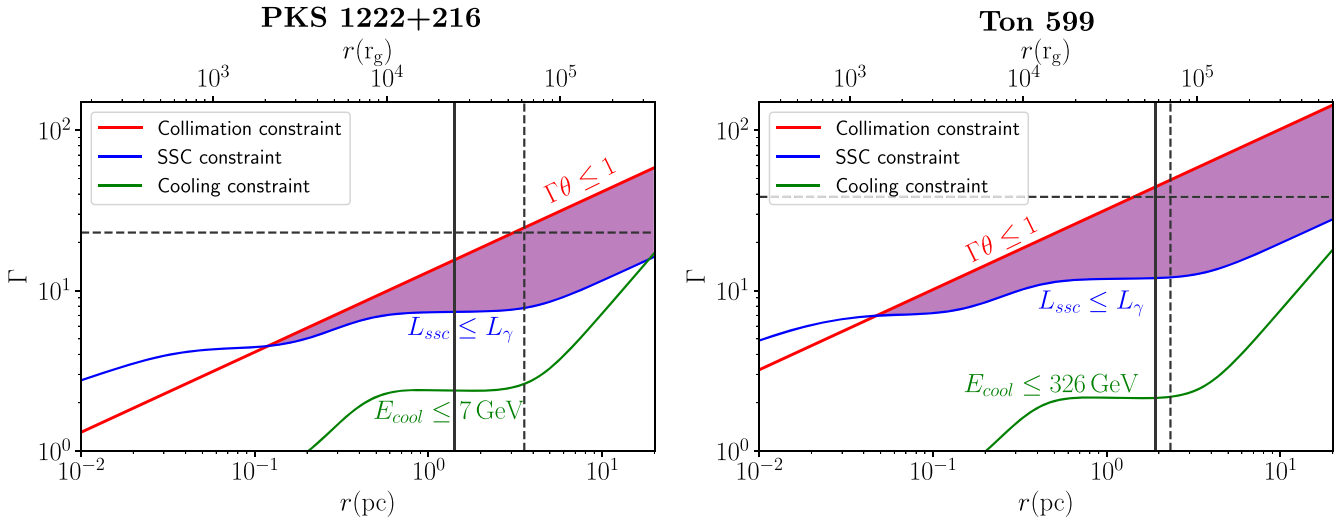

Figure 12. Constraints on the Lorentz factor Γ and distance r between the gamma-ray emission location and central black hole, adapted from Nalewajko et al. (2014). The allowed region is shaded in purple. The black solid vertical line shows the opacity constraint on r derived from the BLR modeling. The values of Γ and r derived from the SED modeling are indicated with dashed black lines.

Table 7
Parameters Used to Calculate Constraints on the Parameter Space

Source	z	D_L (Gpc)	t_{var} (days)	L_{syn} (erg s^{-1})	L_{gamma} (erg s^{-1})	L_d (erg s^{-1})	M_{BH}[a] ($M_{\odot}$)	E_{cool} (GeV)	ϵ_{BLR}[b]	ϵ_{IR}[b]
PKS 1222+216	0.434	2.44	10.0	3.5×10^{46}	7.8×10^{46}	2.8×10^{46}	3.47×10^{8}	7.07	0.02	0.2
Ton 599	0.725	4.54	2.0	4.4×10^{46}	1.2×10^{48}	2.2×10^{46}	6.8×10^{8}	326	0.02	0.2

Notes. Here z and D_L are the redshift and luminosity distance of the source; t_{var} is the variability timescale of cooling derived from each flare's fitted exponential decay; L_{syn}, L_{gamma}, and L_d are the synchrotron, gamma-ray, and disk luminosities from the SED model; M_{BH} is the black hole mass; E_{cool} is the maximum photon energy due to the external Compton cooling of relativistic electrons; and ϵ_{BLR} and ϵ_{IR} are the covering factors of the BLR and IR-emitting torus region, respectively.
[a] Farina et al. (2012); Liu et al. (2006).
[b] Tavecchio et al. (2011).

1.2×10^{46} erg s^{-1} and to be extremely particle-dominated with an equipartition parameter $U_B/U_e = 3.8 \times 10^{-4}$.

8. Lorentz Factors and Locations of the Gamma Ray–Emitting Regions

We determined constraints on the Lorentz factor Γ and distance r of the gamma-ray emission region from the central black hole for PKS 1222+216 and Ton 599 following the method and assumptions of Nalewajko et al. (2014). The constraints are plotted in Figure 12. The parameters used to determine the constraints are given in Table 7. In order to obtain a conservative SSC constraint, we set the SSC luminosity equal to the observed gamma-ray luminosity L_{gamma}. For PKS 1222+216, the fastest variability is observed with Fermi-LAT, while for Ton 599, it is observed with VERITAS. We therefore set the maximum energy E_{cool} for the EIC cooling constraint equal to the geometric mean of the energy ranges observed by Fermi-LAT and VERITAS for the two sources, respectively.

Three constraints on Γ and r are calculated. The collimation constraint requires the size of the emission region to be less than the size of the jet at the emission region location such that $\Gamma\theta \leqslant 1$, where θ as defined by Nalewajko et al. (2014, Equation (1)) is the angle subtended by the blob expanding while propagating.

A caveat of the collimation constraint is the underlying assumption that the blob size is defined by the observed variability such that $R = c\delta t_{\mathrm{var,obs}}/(1+z)$. However, the observed variability only gives an upper limit on the blob radius, meaning that the actual size of the emission zone is likely smaller than that extrapolated from the observed variability. Indeed, our modeling of PKS 1222+216 and Ton 599 predicts an observed variability that is much shorter than the one observed within the reconstructed SED periods. This discrepancy explains why the parameters predicted by our model lie just below the line $\Gamma\theta = 1$.

The SSC constraint requires the SSC luminosity not to exceed the total gamma-ray luminosity, which includes contributions from external radiation fields (Nalewajko et al. 2014, Equation (5)). The cooling constraint requires that electrons radiatively emitting gamma rays at energies above E_{cool} cool through interactions with external radiation fields faster than the flare decay timescale (Nalewajko et al. 2014, Equation (9)).

These parameter limits do not take into account the constraints given by the BLR and dust torus opacity on the gamma-ray emission. In Figure 12, we show with black vertical

lines the minimum distance r from the black hole in the SED models where the BLR would become fully opaque for the maximum observed energy $E_{\rm max}$ (370 GeV for PKS 1222+216 and 630 GeV for Ton 599). We consider the BLR opaque when $\tau_{\rm BLR,E_{max}} > 5$, meaning that less than 1% of the gamma rays can escape. We can clearly see that considering the BLR opacity significantly tightens the constraints on the gamma-ray emission location in Ton 599, as mentioned in the previous section. The opacity constraint on PKS 1222+216 is weaker, as in that case, the blob does not have to be as deep inside the BLR to reproduce the observed EIC emission.

9. Neutrino Emission during VHE Flares

Luminous gamma-ray flares of FSRQs are potential sources of PeV-scale (∼100 TeV–∼10 PeV) neutrino emission (e.g., Mannheim 1993; Dermer et al. 2014; Kadler et al. 2016). While the lack of point sources observed in IceCube data suggests that FSRQs are not the dominant population of neutrino sources, the possibility of neutrino emission during rare, bright flares has not been excluded (Murase & Waxman 2016). While Righi et al. (2020) suggested that the bulk of the average neutrino emission from FSRQs occurs in the sub-EeV–EeV energy range, their results do not exclude PeV-scale neutrino emission during outlier states. In the SED modeling of the VHE flares of PKS 1222+216 and Ton 599 presented here, a purely leptonic model gives an adequate representation of the data, and performing full hadronic modeling is beyond the scope of this work.

However, we can place analytic constraints on the potential PeV-scale neutrino flux produced during these events by considering a leptohadronic scenario in which synchrotron emission from secondary electrons produced by pion decay contributes a subdominant component to the second peak of the SED, similar to models used to describe the flaring emission of TXS 0506+056 coincident with the detection of a neutrino by IceCube (e.g., Keivani et al. 2018; Cerruti et al. 2019; Gao et al. 2019; Reimer et al. 2019). In this section, we make use of the assumptions and methods of Gao et al. (2017), particularly Appendix A of that work. All quantities in the following equations are in the comoving frame of the blob, unless explicitly noted with the superscript "ob."

We consider neutrinos produced by the $p\gamma$ interaction via the $\Delta^+(1232)$ resonance with threshold energy $\epsilon_{p\gamma,\rm th} \sim 0.3$ GeV. The characteristic proton energy is $E_{p,\rm char} \sim E_\nu/K_\nu \sim 2$ PeV, where $E_\nu = E_\nu^{\rm ob}(1+z)/\Gamma$ and $K_\nu \sim 0.05$ (Murase et al. 2014). Therefore, to check whether these sources could, in principle, support PeV neutrino emission, we first estimate the maximum energy to which protons can be accelerated in the source without escaping, following Hillas (1984), as

$$E_{p,\rm max} = Ze\beta cBR, \tag{11}$$

where the atomic number $Z = 1$ for protons, e is the elementary charge, $\beta = v/c \sim 1$ for highly relativistic particles, c is the speed of light, B is the magnetic field in the source, and R is the size of the source. Using the values in Table 6, the maximum energy to which protons could have been accelerated in the gamma-ray emission regions for the flares of PKS 1222+216 and Ton 599 is $E_p \sim 500$ PeV, equivalent to an upper limit on the neutrino energy of $E_\nu^{\rm ob} \sim 400$ PeV, so PeV-scale neutrino emission is certainly feasible.

A limit on the neutrino flux can be imposed by considering a steady state within the time period of the flare in which the synchrotron luminosity of the secondary electrons equals the power injected by pion decay. Because the lifetime of the ultra-high-energy (UHE) protons cooling by photopion production may be longer than that of the electrons, the resulting model can be considered to provide an upper limit on the neutrino luminosity. The steady-state proton energy density at $E_{p,\rm char}$ is given by Gao et al. (2017),

$$u_p(E_{p,\rm char}) = \frac{\alpha_{\rm fs}\,\epsilon_{p\gamma,\rm th}}{c\sigma_{p\gamma}K_{p\gamma}K_{\pi\to e}}\frac{m_pc^2}{E_{p,\rm char}}\frac{\nu F_{\nu,2}^{\rm ob}}{\nu F_{\nu,\rm t}^{\rm ob}}, \tag{12}$$

where $\alpha_{\rm fs} = 4c/(3R)$ is the free-streaming escape rate, $\sigma_{p\gamma} = 5.0\times10^{-28}\,{\rm cm}^2$ is the $p\gamma$ cross section, $K_{p\gamma} \sim 0.2$ is the average inelasticity for the proton in the $p\gamma$ interaction, $K_{\pi\to e} \sim 1/8$ is the fraction of energy transferred to $e^\pm$ pairs from pion decay, $\nu F_{\nu,2}^{\rm ob}$ is the observed flux due to synchrotron emission from the secondary electrons, and $\nu F_{\nu,\rm t}^{\rm ob}$ is the observed flux of the target photons of the $p\gamma$ interaction at $E_{\rm t} \sim \epsilon_{p\gamma,\rm th}m_pc^2/E_{p,\rm char}$, which is directly constrained by the Swift-XRT measurement at $E_{\rm t}\Gamma/(1+z) \sim 2$keV. We can estimate $\nu F_{\nu,2}^{\rm ob}$ from the SED at the synchrotron peak frequency of the secondary electrons at

$$\begin{aligned}\nu_2^{\rm ob} &= \frac{ce(K_{p\gamma}K_{\pi\to e})^2}{2\pi(m_ec^2)^3}\frac{\Gamma}{1+z}BE_{p,\rm char}\\ &\approx 10^{22}\left(\frac{\Gamma}{23}\right)\left(\frac{B}{30\ {\rm mG}}\right)\left(\frac{E_{p,\rm char}}{2\ {\rm PeV}}\right){\rm Hz}\end{aligned} \tag{13}$$

for redshift $z \sim 0.5$. The corresponding power in protons can be estimated as

$$L_p \sim \Gamma^2 u_p(E_{p,\rm char})\alpha_{\rm esc}V(R), \tag{14}$$

where, for simplicity, we assume the proton escape time $\alpha_{\rm esc} = 0.1\alpha_{\rm fs}$ and let $V(R) = 4\pi R^3/3$ for a spherical blob. Parameterizing this power by the Eddington luminosity boosted into the jet frame yields

$$\begin{aligned}L_p \sim 1&\left(\frac{\Gamma}{23}\right)^2\left(\frac{R}{6\times10^{16}\ {\rm cm}}\right)\left(\frac{M}{5\times10^{10}\,M_\odot}\right)^{-1}\\ &\times\left(\frac{E_{p,\rm char}}{2\ {\rm PeV}}\right)^{-1}\left(\frac{\nu F_{\nu,2}^{\rm ob}/\nu F_{\nu,\rm t}^{\rm ob}}{0.5}\right)L_{\rm Edd},\end{aligned} \tag{15}$$

where $\nu F_{\nu,2}^{\rm ob} \lesssim 0.5\,\nu F_{\nu,\rm t}^{\rm ob} \sim 1\times10^{-12}\,{\rm erg\,cm^{-2}\,s^{-1}}$ is a conservative estimate of the largest energetically reasonable contribution[50] to the SED at $\sim10^{22}$ Hz. The contribution is clearly subdominant. We can then estimate the observed neutrino energy flux, where $\dot{N}_{p\gamma}$ is the $p\gamma$ event rate per physical volume, using the relation

$$\dot{N}_{p\gamma} \sim c\sigma_{p\gamma}\frac{u_{\rm ph}(E_{\rm t})}{E_{\rm t}}\frac{u_p(E_{p,\rm char})}{E_{p,\rm char}} = \frac{\alpha_{\rm fs}u_\nu(E_\nu)}{E_\nu}, \tag{16}$$

[50] This assumption requires about 5×10^{-3} protons for every electron from Equation (12) and the electron energy distributions reported in Table 6.

where $u_{\rm ph}(E_{\rm t})$ is the energy density of the target photons. Since $u_{\nu}(E_{\nu})\big/u_{\rm ph}(E_{\rm t}) = \nu F^{\rm ob}_{\nu,\nu}\big/\nu F^{\rm ob}_{\nu,{\rm t}}$, we obtain the simple relation

$$\nu F^{\rm ob}_{\nu,\nu} = \frac{K_{\nu}}{K_{p\gamma}K_{\pi\to e}}\nu F^{\rm ob}_{\nu,2} \sim 2\ \nu F^{\rm ob}_{\nu,2}. \tag{17}$$

The number of PeV-scale neutrinos of any flavor expected to be detected by IceCube during the VHE flare of PKS 1222+216 or Ton 599 is then

$$N_{\nu} \lesssim 0.001\left(\frac{\nu F^{\rm ob}_{\nu,\nu}}{2\times 10^{-12}\ {\rm erg\ cm^{-2}\ s^{-1}}}\right) \times \left(\frac{\Delta T}{5\ {\rm days}}\right)\left(\frac{\mathcal{A}_{\rm eff}}{10^{6}\ {\rm cm^{2}}}\right), \tag{18}$$

where ΔT is the duration of the VHE flare, $\mathcal{A}_{\rm eff} \sim 10^{6}\ {\rm cm^{2}}$ is the IceCube effective area for extremely high-energy (EHE) real-time alerts in the PeV range (Aartsen et al. 2017), and $\Delta\nu \sim \ln(10)$ is assumed for the width of the neutrino spectrum. We conclude that it is plausible that PKS 1222+216 and Ton 599 could have produced PeV-scale neutrinos during their VHE flaring activity at a flux consistent with a null detection by current instruments.

To reduce the model dependence of our constraints, R could also be estimated using the timescale of gamma-ray flare variability,

$$R \sim \frac{\delta}{1+z}c\Delta T, \tag{19}$$

from which estimates of $R \sim 7\times 10^{17}$ and 1×10^{17} cm are obtained for PKS 1222+216 and Ton 599. For the two sources, the constraints on the maximum neutrino energy are loosened to $E^{\rm ob}_{\nu} \sim 5$ EeV and 700 PeV, respectively, and the required proton luminosities are increased by a factor of ∼10 and ∼2, or within a few times the Eddington luminosity for both sources.

10. Conclusions

In this paper, we present an analysis of the gamma-ray and multiwavelength emission of three bright, variable FSRQs observed by Fermi-LAT and VERITAS, 3C 279, PKS 1222+216, and Ton 599, making use of almost 100 hr of VERITAS observations of these sources. No VHE gamma-ray activity was observed during multiple flares of 3C 279, which is the brightest of the three sources as observed with Fermi-LAT, but VERITAS detected flares of both PKS 1222+216 and Ton 599.

The flux distributions of the Fermi-LAT light curves of all three sources are consistent with the PDF derived from the SDE proposed by Tavecchio et al. (2020), in which the timescale of variability is controlled by processes in the accretion disk. The timescales associated with magnetorotational instabilities and magnetic flux accumulation in the accretion disk obtained from this model are consistent with theoretical estimates.

We selected gamma-ray flaring states from the Fermi-LAT light curves of the three sources using a procedure based on Bayesian blocks. Daily to subdaily variability was observed by Fermi-LAT during the flaring states. No pattern of asymmetry was found in the rise and decay times of the exponential components of the 10 identified flares of 3C 279, while the fluence distribution of the flare components extended over 1 order of magnitude.

All three sources have similar gamma-ray spectra consistent with a log-parabola model. The average flaring spectrum of 3C 279 was found to exhibit stronger curvature than the baseline state, consistent with a null VHE detection even during extremely bright flares.

The SEDs of the VHE flares of PKS 1222+216 and Ton 599 are described well by a purely leptonic emission model including an EIC emission component. For both sources, a strong constraint was placed on the Doppler factor, which must be $\gtrsim$40 for PKS 1222+216 and $\gtrsim$50 for Ton 599, to produce the observed gamma-ray emission at up to TeV energies despite internal absorption. We constrained the jet Lorentz factor and distance of the gamma-ray emission region from the central black hole using the independent method of Nalewajko et al. (2014), which we augmented using an opacity constraint derived from our SED modeling. We found that both sources are operating in a similar regime, with both of them having strongly matter-dominated energetics and a gamma-ray emission zone located a few parsecs from the SMBH. It would be interesting in future work to extend this study to a large sample of TeV FSRQs in order to define the common physical properties of this blazar subclass.

We calculated analytic constraints on a supposed subdominant hadronic component to the leptonic SED model, from which we estimated upper limits on potential PeV-scale neutrino emission during the TeV flares. We found that neutrino emission is energetically plausible at a flux consistent with a null detection by IceCube during the TeV flares.

This research is supported by grants from the US Department of Energy Office of Science, the US National Science Foundation, and the Smithsonian Institution; NSERC in Canada; and the Helmholtz Association in Germany. This research used resources provided by the Open Science Grid, which is supported by the National Science Foundation and the US Department of Energy's Office of Science, and resources of the National Energy Research Scientific Computing Center (NERSC), a US Department of Energy Office of Science User Facility operated under contract No. DE-AC02-05CH11231. We acknowledge the excellent work of the technical support staff at the Fred Lawrence Whipple Observatory and the collaborating institutions in the construction and operation of the instrument.

The Fermi-LAT Collaboration acknowledges generous ongoing support from a number of agencies and institutes that have supported both the development and the operation of the LAT, as well as scientific data analysis. These include the National Aeronautics and Space Administration and the Department of Energy in the United States, the Commissariat à l'Energie Atomique and the Centre National de la Recherche Scientifique/Institut National de Physique Nucléaire et de Physique des Particules in France, the Agenzia Spaziale Italiana and the Istituto Nazionale di Fisica Nucleare in Italy, the Ministry of Education, Culture, Sports, Science and Technology (MEXT), High Energy Accelerator Research Organization (KEK), and Japan Aerospace Exploration Agency (JAXA) in Japan, and the K. A. Wallenberg Foundation, the Swedish Research Council, and the Swedish National Space Board in Sweden.

Additional support for science analysis during the operations phase is gratefully acknowledged from the Istituto Nazionale di Astrofisica in Italy and the Centre National d'Études Spatiales in France. This work was performed in part under DOE contract DE-AC02-76SF00515.

Data from the Steward Observatory spectropolarimetric monitoring project were used. This program is supported by Fermi Guest Investigator grants NNX08AW56G, NNX09AU10G, NNX12AO93G, and NNX15AU81G. L.S. acknowledges support from the Sloan Fellowship, the Cottrell Scholars Award, DoE DE-SC0016542, NASA 80NSSC18K1104, and NSF PHY-1903412. This material is based upon work supported in part by the National Science Foundation under grant PHY-1659528.

A.B.'s work was supported by NSF grant PHY-1806554 at Barnard College, Columbia University. O.H. thanks NSF for support under grants PHY-1707432 and PHY-2011420. J.V. was partially supported by the Alliance program, a partnership between Columbia University, NY, USA, and three major French institutions: École Polytechnique, Paris 1 Panthéon-Sorbonne University, and Science Po. This material is based upon work supported by NASA under award No. 80GSFC21M0002. S.B. acknowledges financial support by the European Research Council for the ERC starting grant MessMapp under contract No. 949555.

This work made use of the online cosmological calculator of Wright (2006) and NASA's Astrophysics Data System. We would like to thank the anonymous referee for the helpful and timely comments that helped improve the quality of the paper.

Software: Astropy (Astropy Collaboration et al. 2013, 2018), Fermitools (Fermi Science Support Development Team 2019), NumPy (Harris et al. 2020), Matplotlib (Hunter 2007), SciPy (Virtanen et al. 2020).

Appendix A
Complete Set of Fermi-LAT Flare Profiles for 3C 279

Figure 13 shows the Fermi-LAT subdaily light curves for all 10 selected flares, along with the VERITAS upper limits during those times. The results of the Fermi-LAT flare profile fits for those flares are given in Table 8.

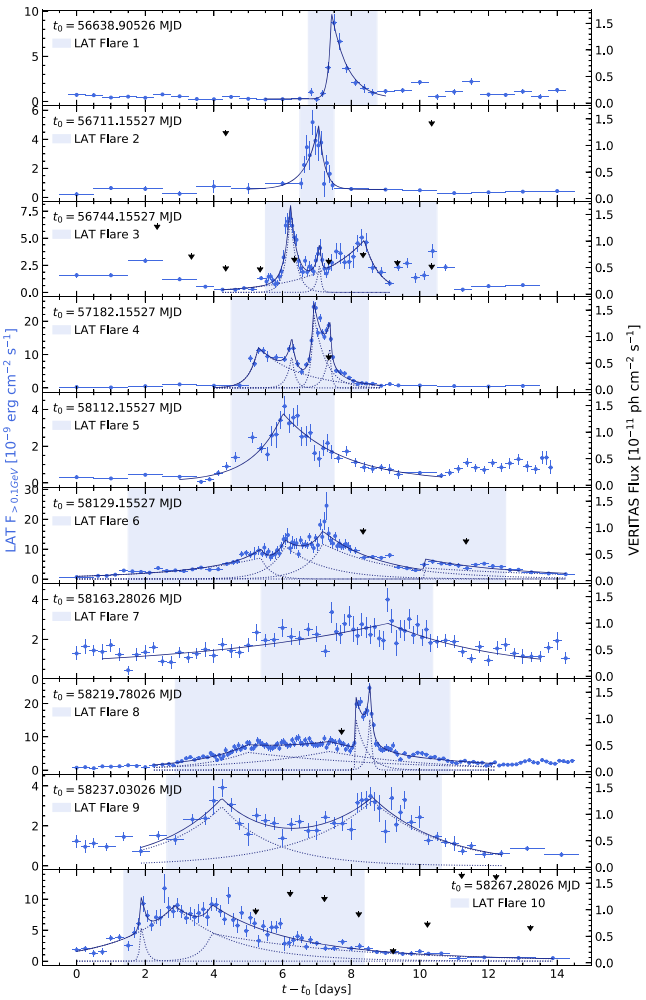

Figure 13. The 3C 279 LAT subdaily light curves (blue points) around the flaring episodes selected as described in Section 4 (shaded areas). The dotted blue lines show the fitted exponential profiles, with their sums shown in solid blue. The VERITAS 95% upper limits are shown as black downward arrows. For flares 1, 5, 7, and 9, no VERITAS observations were taken around the time of the flare.

Table 8
Results of the LAT Flare Profile Fits for 3C 279

Amplitude (F_0) (10^{-9} erg cm^{-2} s^{-1})	t_{peak} (MJD)	t_{rise} (minutes)	t_{decay} (minutes)	Constant ($F_{const.}$) (10^{-9} erg cm^{-2} s^{-1})
Flare 1 (MJD 56,645.655–56,647.655): χ^2/d.o.f. = 12.05/8 = 1.51				
9.56 ± 1.07	$56{,}646.330 \pm 0.033$	130 ± 45	674 ± 73	0.28 ± 0.06
Flare 2 (MJD 56,717.655–56,718.655): χ^2/d.o.f. = 16.63/10 = 1.66				
4.40 ± 0.70	$56{,}718.142 \pm 0.043$	445 ± 95	307 ± 86	0.55 ± 0.07
Flare 3 (MJD 56,749.655–56,754.655): χ^2/d.o.f. = 69.98/34 = 2.06				
7.27 ± 0.64	$56{,}750.382 \pm 0.015$	229 ± 25	267 ± 42	N.A.
2.78 ± 1.15	$56{,}751.238 \pm 0.024$	140 ± 82	69 ± 47	N.A.
4.80 ± 0.37	$56{,}752.532 \pm 0.067$	2001 ± 116	631 ± 136	N.A.
Flare 4 (MJD 57,186.655–57,190.655): χ^2/d.o.f. = 77.31/19 = 4.07				
12.07 ± 0.67	$57{,}187.446 \pm 0.031$	378 ± 46	1784 ± 147	N.A.
9.79 ± 2.29	$57{,}188.425 \pm 0.028$	216 ± 101	155 ± 64	N.A.
21.72 ± 1.59	$57{,}189.069 \pm 0.008$	137 ± 18	512 ± 55	N.A.
12.41 ± 1.30	$57{,}189.532 \pm 0.010$	220 ± 63	77 ± 25	N.A.
Flare 5 (MJD 58,116.655–58,119.655): χ^2/d.o.f. = 54.70/29 = 1.89				
3.72 ± 0.20	$58{,}118.171 \pm 0.069$	1278 ± 220	2521 ± 309	0.06 ± 0.11
Flare 6 (MJD 58,130.655–58,141.655): χ^2/d.o.f. = 141.28/72 = 1.96				
7.08 ± 1.01	$58{,}134.520 \pm 0.055$	3719 ± 390	421 ± 259	N.A.
10.95 ± 3.74	$58{,}135.229 \pm 0.053$	718 ± 232	3535 ± 1394	N.A.
11.78 ± 7.00	$58{,}136.266 \pm 0.048$	349 ± 160	1839 ± 1055	N.A.
3.44 ± 0.66	$58{,}139.546 \pm 0.033$	233 ± 175	6119 ± 1824	N.A.
Flare 7 (MJD 58,168.655–58,173.655): χ^2/d.o.f. = 78.81/58 = 1.36				
2.36 ± 0.50	$58{,}172.345 \pm 0.242$	8540 ± 4159	4458 ± 2319	0.45 ± 0.59
Flare 8 (MJD 58,222.655–58,230.655): χ^2/d.o.f. = 177.25/106 = 1.67				
5.29 ± 1.29	$58{,}224.773 \pm 0.105$	1996 ± 716	5899 ± 4035	N.A.
17.70 ± 2.01	$58{,}227.945 \pm 0.004$	$\mathbf{36 \pm 13}$	329 ± 131	N.A.
16.42 ± 1.87	$58{,}228.323 \pm 0.012$	140 ± 54	115 ± 48	N.A.
5.59 ± 1.69	$58{,}227.139 \pm 0.133$	3816 ± 1450	4077 ± 2080	N.A.
Flare 9 (MJD 58,239.655–58,247.655): χ^2/d.o.f. = 46.25/34 = 1.36				
2.96 ± 0.40	$58{,}241.258 \pm 0.149$	2546 ± 595	2226 ± 1088	N.A.
3.27 ± 0.25	$58{,}245.648 \pm 0.133$	3080 ± 1384	3028 ± 303	N.A.
Flare 10 (MJD 58,268.655–58,275.655): χ^2/d.o.f. = 75.80/55 = 1.37				
6.23 ± 9.46	$58{,}269.171 \pm 0.182$	73 ± 236	177 ± 102	N.A.
8.81 ± 0.84	$58{,}270.137 \pm 0.107$	2392 ± 243	2449 ± 956	N.A.
4.46 ± 1.91	$58{,}271.223 \pm 0.088$	477 ± 431	5824 ± 862	N.A.

Note. The smallest variability time found is indicated in bold.

Appendix B
Fermi-LAT Spectral Fit Parameters

Table 9 provides the Fermi-LAT spectral fit parameters for 3C 279, PKS 1222+216, and Ton 599.

Table 9
Fermi-LAT Spectral Fit Parameters

State	Epoch (MJD)	TS	N_0 (10^{-10} MeV^{-1} cm^{-2} s^{-1})	α	β ($\times 10^{-2}$)	Flux (10^{-6} ph cm^{-2} s^{-1})
			3C 279			
Global	54,682.66–58,459.35	271,945	3.33 ± 0.02	2.228 ± 0.004	6.1 ± 0.3	0.751 ± 0.004
Low state	56,230.66–56,465.66	1130	0.54 ± 0.03	2.38 ± 0.06	2.9 ± 3.1	0.14 ± 0.01
VER-LAT quiescent	Various	322	5.7 ± 0.8	2.2 ± 0.1	1.8 ± 7.0	1.4 ± 0.2
LAT flares simultaneous with VER obs.	56,750.27–56,750.34	578	69 ± 10	2.1 ± 0.1	31 ± 13	11 ± 2
	57,189.17–57,189.23	1141	173 ± 15	2.07 ± 0.07	14 ± 6	32 ± 3
	58,227.22–58,227.27	355	79 ± 14	1.8 ± 0.2	21 ± 13	12 ± 4
	58,272.18–58,272.22	235	62 ± 15	1.5 ± 0.3	42 ± 2	7 ± 3
LAT flares	56,645.66–56,647.66	1633	22.0 ± 1.5	1.73 ± 0.07	9.6 ± 3.2	3.7 ± 0.3
	56,717.66–56,718.66	900	23.2 ± 2.0	2.08 ± 0.08	11 ± 6	4.5 ± 0.5
	56,749.66–56,754.66	7680	24.0 ± 0.8	2.20 ± 0.03	13 ± 2	5.0 ± 0.2
	57,186.66–57,190.66	23,623	77.9 ± 1.5	2.04 ± 0.02	11 ± 1	14.7 ± 0.5
	58,116.66–58,119.66	3543	19.5 ± 0.9	2.06 ± 0.04	4.1 ± 2.2	4.0 ± 0.2
	58,130.66–58,141.66	27,256	53.3 ± 0.9	2.14 ± 0.02	8.5 ± 1.1	11.0 ± 0.2
	58,168.66–58,173.66	4932	19.5 ± 0.7	2.10 ± 0.03	5.8 ± 2.0	4.1 ± 0.2
	58,222.66–58,230.66	53,745	59.4 ± 0.7	2.00 ± 0.01	9.6 ± 0.7	11.2 ± 0.1
	58,239.66–58,247.66	7989	19.2 ± 0.6	1.90 ± 0.03	6.2 ± 1.4	3.6 ± 0.1
	58,268.66–58,275.66	107,456	47.8 ± 1.3	1.91 ± 0.02	14 ± 2	8.2 ± 0.2
			PKS 1222+216			
Global	54,682.66–58,459.64	94,556	1.66 ± 0.01	2.305 ± 0.007	3.8 ± 0.4	0.337 ± 0.002
			Ton 599			
Global	54,682.66–58,464.49	48,176	6.55 ± 0.06	2.11 ± 0.01	5.5 ± 0.5	0.161 ± 0.002

ORCID iDs

C. B. Adams https://orcid.org/0000-0002-9021-6192
W. Benbow https://orcid.org/0000-0003-2098-170X
A. Brill https://orcid.org/0000-0002-6208-5244
M. Errando https://orcid.org/0000-0002-1853-863X
Q. Feng https://orcid.org/0000-0001-6674-4238
L. Fortson https://orcid.org/0000-0002-1067-8558
A. Furniss https://orcid.org/0000-0003-1614-1273
A. Gent https://orcid.org/0000-0001-7429-3828
D. Hanna https://orcid.org/0000-0002-8513-5603
T. Hassan https://orcid.org/0000-0002-4758-9196
O. Hervet https://orcid.org/0000-0003-3878-1677
W. Jin https://orcid.org/0000-0002-1089-1754
P. Kaaret https://orcid.org/0000-0002-3638-0637
D. Kieda https://orcid.org/0000-0003-4785-0101
G. Maier https://orcid.org/0000-0001-9868-4700
P. Moriarty https://orcid.org/0000-0002-1499-2667
R. Mukherjee https://orcid.org/0000-0002-3223-0754
R. A. Ong https://orcid.org/0000-0002-4837-5253
A. N. Otte https://orcid.org/0000-0002-5955-6383
K. Pfrang https://orcid.org/0000-0002-7990-7179
M. Pohl https://orcid.org/0000-0001-7861-1707
E. Pueschel https://orcid.org/0000-0002-0529-1973
J. Quinn https://orcid.org/0000-0002-4855-2694
K. Ragan https://orcid.org/0000-0002-5351-3323
D. Ribeiro https://orcid.org/0000-0002-7523-7366
J. L. Ryan https://orcid.org/0000-0001-6662-5925
M. Santander https://orcid.org/0000-0001-7297-8217
D. A. Williams https://orcid.org/0000-0003-2740-9714
C. C. Cheung https://orcid.org/0000-0002-4377-0174
S. Ciprini https://orcid.org/0000-0002-0712-2479
D. Gasparrini https://orcid.org/0000-0002-5064-9495
L. Sironi https://orcid.org/0000-0002-1227-2754

References

Aartsen, M., Ackermann, M., Adams, J., et al. 2017, APh, 92, 30
Abdo, A. A., Ackermann, M., Ajello, M., et al. 2010, ApJ, 722, 520
Abdo, A. A., Ackermann, M., Ajello, M., et al. 2011, ApJ, 734, 116
Abdo, A. A., Ackermann, M., Ajello, M., et al. 2012, ApJ, 758, 140
Abdollahi, S., Acero, F., Ackermann, M., et al. 2020, ApJS, 247, 33
Abeysekara, A. U., Archambault, S., Archer, A., et al. 2015, ApJL, 815, L22
Abolmasov, P., & Poutanen, J. 2017, MNRAS, 464, 152
Ackermann, M., Anantua, R., Asano, K., et al. 2016, ApJL, 824, L20
Aharonian, F. A. 2000, NewA, 5, 377
Aharonian, F., Akhperjanian, A. G., Bazer-Bachi, A. R., et al. 2007, ApJL, 664, L71
Aitchison, J., & Brown, A. C. 1973, The Lognormal Distribution (Cambridge: Cambridge Univ. Press), 104
Ajello, M., Angioni, R., Axelsson, M., et al. 2020, ApJ, 892, 105
Aleksić, J., Antonelli, L. A., Antoranz, P., et al. 2011, ApJL, 730, L8

Astropy Collaboration, Price-Whelan, A. M., SipHocz, B. M., et al. 2018, AJ, 156, 123
Astropy Collaboration, Robitaille, T. P., Tollerud, E. J., et al. 2013, A&A, 558, A33
Atwood, W., Albert, A., Baldini, L., et al. 2013, arXiv:1303.3514
Atwood, W. B., Abdo, A. A., Ackermann, M., et al. 2009, ApJ, 697, 1071
Ballet, J., Burnett, T. H., Digel, S. W., & Lott, B. 2020, arXiv:2005.11208
Barbiellini, G., Bastieri, D., Bechtol, K., et al. 2014, ApJ, 784, 118
Bennett, C. L., Larson, D., Weiland, J. L., & Hinshaw, G. 2014, ApJ, 794, 135
Blandford, R. D., & Königl, A. 1979, ApJ, 232, 34
Bruel, P., Burnett, T. H., Digel, S. W., et al. 2018, arXiv:1810.11394
Burbidge, E. M. 1968, ApJL, 154, L109
Burrows, D. N., Hill, J. E., Nousek, J. A., et al. 2005, SSRv, 120, 165
Cerruti, M., Zech, A., Boisson, C., et al. 2019, MNRAS, 483, L12
Cheung, C. C., Gasparrini, D., & Buson, S. 2017, ATel, 10931, 1
Cogan, P. 2007, in Proc. of the 30th Int. Cosmic Ray Conf. (New York: AIP), 1385
Costamante, L., Cutini, S., Tosti, G., Antolini, E., & Tramacere, A. 2018, MNRAS, 477, 4749
Dermer, C. D., & Menon, G. 2009, High Energy Radiation from Black Holes: Gamma Rays, Cosmic Rays, and Neutrinos (Princeton, NJ: Princeton Univ. Press)
Dermer, C. D., Murase, K., & Inoue, Y. 2014, JHEAp, 3, 29
Emery, G., Cerruti, M., Dmytriiev, A., et al. 2019, in 36th Int. Cosmic Ray Conf. (ICRC2019) (New York: AIP), 668
Errando, M. 2014, AAS/High Energy Astrophysics Division, 14, 106.11
Fanaroff, B. L., & Riley, J. M. 1974, MNRAS, 167, 31P
Farina, E. P., Decarli, R., Falomo, R., Treves, A., & Raiteri, C. M. 2012, MNRAS, 424, 393
Fermi Science Support Development Team 2019, Fermitools: Fermi Science Tools, Astrophysics Source Code Library, ascl:1905.011
Fossati, G., Maraschi, L., Celotti, A., Comastri, A., & Ghisellini, G. 1998, MNRAS, 299, 433
Franceschini, A., & Rodighiero, G. 2017, A&A, 603, A34
Gao, S., Fedynitch, A., Winter, W., & Pohl, M. 2019, NatA, 3, 88
Gao, S., Pohl, M., & Winter, W. 2017, ApJ, 843, 109
Gehrels, N., Chincarini, G., Giommi, P., et al. 2004, ApJ, 611, 1005
Ghisellini, G., Celotti, A., Fossati, G., Maraschi, L., & Comastri, A. 1998, MNRAS, 301, 451
Ghisellini, G., & Madau, P. 1996, MNRAS, 280, 67
Ghisellini, G., & Tavecchio, F. 2009, MNRAS, 397, 985
Giannios, D., & Uzdensky, D. A. 2019, MNRAS, 484, 1378
Giebels, B., & Degrange, B. 2009, A&A, 503, 797
Harris, C. R., Millman, K. J., van der Walt, S. J., et al. 2020, Natur, 585, 357
Hayashida, M., Nalewajko, K., Madejski, G. M., et al. 2015, ApJ, 807, 79
Hervet, O., Boisson, C., & Sol, H. 2015, A&A, 578, A69
Hervet, O., Boisson, C., & Sol, H. 2016, A&A, 592, A22
Hillas, A. M. 1984, ARA&A, 22, 425
Holder, J. 2011, in Proc. of the 32nd Int. Cosmic Ray Conf. (ICRC2011) (New York: AIP), 137
Holder, J. 2014, ATel, 5981, 1
Hunter, J. D. 2007, CSE, 9, 90
IceCube Collaboration, Aartsen, M. G., Ackermann, M., et al. 2018, Sci, 361, eaat1378
Inoue, S., & Takahara, F. 1996, ApJ, 463, 555
Johannesson, G., & Orlando, E. 2013, in Proc. of the 33rd Int. Cosmic Ray Conf. (ICRC2013) (New York: AIP), 3106
Jorstad, S. G., Marscher, A. P., Mattox, J. R., et al. 2001, ApJS, 134, 181
Kadler, M., Krauß, F., Mannheim, K., et al. 2016, NatPh, 12, 807
Kalberla, P. M. W., Burton, W. B., Hartmann, D., et al. 2005, A&A, 440, 775
Katarzyński, K., Sol, H., & Kus, A. 2001, A&A, 367, 809
Keenan, M., Meyer, E. T., Georganopoulos, M., Reddy, K., & French, O. J. 2021, MNRAS, 505, 4726
Keivani, A., Murase, K., Petropoulou, M., et al. 2018, ApJ, 864, 84
Krause, M., Pueschel, E., & Maier, G. 2017, APh, 89, 1
Liu, Y., Jiang, D. R., & Gu, M. F. 2006, ApJ, 637, 669
Lynds, C. R., Stockton, A. N., & Livingston, W. C. 1965, ApJ, 142, 1667
Maier, G., & Holder, J. 2017, in Proc. of the 35th Int. Cosmic Ray Conf. (ICRC 2017) (New York: AIP), 747
Mannheim, K. 1993, A&A, 269, 67
Maraschi, L., Ghisellini, G., & Celotti, A. 1992, ApJL, 397, L5
Meyer, M., Scargle, J. D., & Blandford, R. D. 2019, ApJ, 877, 39
Mirzoyan, R. 2017, ATel, 11061, 1
Mücke, A., & Protheroe, R. J. 2000, in AIP Conf. Ser., 515, ed. B. L. Dingus, M. H. Salamon, & D. B. Kieda (Melville, NY: AIP), 149
Mukherjee, R. 2001, in AIP Conf. Proc., 558 (Melville, NY: AIP), 324
Mukherjee, R. 2017, ATel, 11075, 1
Murase, K., Inoue, Y., & Dermer, C. D. 2014, PhRvD, 90, 1
Murase, K., & Waxman, E. 2016, PhRvD, 94, 103006
Nalewajko, K., Begelman, M. C., & Sikora, M. 2014, ApJ, 789, 161
Nieppola, E., Valtaoja, E., Tornikoski, M., Hovatta, T., & Kotiranta, M. 2008, A&A, 488, 867
Osterbrock, D. E., & Pogge, R. W. 1987, ApJ, 323, 108
Padovani, P., Oikonomou, F., Petropoulou, M., Giommi, P., & Resconi, E. 2019, MNRAS, 484, L104
Patel, S. R., & Chitnis, V. R. 2020, MNRAS, 492, 72
Petropoulou, M., Giannios, D., & Sironi, L. 2016, MNRAS, 462, 3325
Poole, T. S., Breeveld, A. A., Page, M. J., et al. 2008, MNRAS, 383, 627
Prince, R. 2019, ApJ, 871, 101
Prince, R. 2020, ApJ, 890, 164
Reimer, A., Böttcher, M., & Buson, S. 2019, ApJ, 881, 46
Resconi, E., Franco, D., Gross, A., Costamante, L., & Flaccomio, E. 2009, A&A, 502, 499
Righi, C., Palladino, A., Tavecchio, F., & Vissani, F. 2020, A&A, 642, A92
Roming, P. W. A., Kennedy, T. E., Mason, K. O., et al. 2005, SSRv, 120, 95
Roming, P. W. A., Koch, T. S., Oates, S. R., et al. 2009, ApJ, 690, 163
Romoli, C., Zacharias, M., Meyer, M., et al. 2017, in Proc. of the 35th Int. Cosmic Ray Conf. (ICRC2017) (New York: AIP), 649
Roy, N., Chatterjee, R., Joshi, M., & Ghosh, A. 2019, MNRAS, 482, 743
Scargle, J. D., Norris, J. P., Jackson, B., & Chiang, J. 2013, ApJ, 764, 167
Schlafly, E. F., & Finkbeiner, D. P. 2011, ApJ, 737, 103
Schneider, D. P., Richards, G. T., Hall, P. B., et al. 2010, AJ, 139, 2360
Shah, Z., Mankuzhiyil, N., Sinha, A., et al. 2018, RAA, 18, 141
Sikora, M., Stawarz, Ł., Moderski, R., Nalewajko, K., & Madejski, G. M. 2009, ApJ, 704, 38
Sinha, A., Sahayanathan, S., Acharya, B. S., et al. 2017, ApJ, 836, 83
Smith, P. S., Montiel, E., Rightley, S., et al. 2009, arXiv:0912.3621
Tavecchio, F., Becerra-Gonzalez, J., Ghisellini, G., et al. 2011, A&A, 534, A86
Tavecchio, F., Bonnoli, G., & Galanti, G. 2020, MNRAS, 497, 1294
Valtaoja, E., Lähteenmäki, A., Teräsranta, H., & Lainela, M. 1999, ApJS, 120, 95
Virtanen, P., Gommers, R., Oliphant, T. E., et al. 2020, NatMe, 17, 261
Wehrle, A. E., Pian, E., Urry, C. M., et al. 1998, ApJ, 497, 178
Wilcoxon, F. 1945, Biometrics Bulletin, 1, 80
Willingale, R., Starling, R. L. C., Beardmore, A. P., Tanvir, N. R., & O'Brien, P. T. 2013, MNRAS, 431, 394
Wright, E. L. 2006, PASP, 118, 1711
Yoo, S., & An, H. 2020, ApJ, 902, 2